Efficient Tunnel Detection with Waveform Inversion of Back-scattered Surface Waves

By

Yao Wang

M.D., University of Kansas, 2015
B.S., China University of Geosciences, 2011

Submitted to the graduate degree program in Department of Mathematics and the Graduate Faculty of the University of Kansas in partial fulfillment of the requirements for the degree of Master of Arts.

_____

Chair: Dr. Xuemin Tu

_____

Dr. Hongguo Xu

_____

Dr. Georgios P. Tsoflias

Date Defended: 10 May 2019

The thesis committee for Yao Wang certifies that this is the approved version of the following thesis:

Efficient Tunnel Detection with Waveform Inversion of Back-scattered Surface Waves

_____

Chair: Dr. Xuemin Tu

Date Approved: 10 May 2019

Abstract

An efficient subsurface imaging method employing back-scattered surface waves is developed to detect near-surface underground elastic-wave velocity anomalies, such as tunnels, sinkholes, fractures, faults, and abandoned manmade infrastructures. The back-scattered surface waves are generated by seismic waves impinging on the velocity anomalies and diffracting back toward the source. These wave events contain plentiful information of the subsurface velocity anomalies including spatial location, shape, size, and velocity of the interior medium. Studies have demonstrated that the back-scattered surface waves can be easily distinguished in the frequency-wavenumber (F-k) domain and have less interference by other wave modes. Based on these features, a near-surface velocity anomaly detection method by using waveform inversion of the back-scattered surface waves (BSWI) is proposed. The main objective of this thesis is to review the theoretical background and study the feasibility of the proposed BSWI method.

The proposed BSWI method is tested with numerical and real-world examples. First, the numerical example uses the conventional full-waveform inversion (FWI) method as a benchmark to demonstrate the efficiency of BSWI method in detecting shallow velocity anomalies. Then, the BSWI method is tested with field data. In this study, 2D seismic data were acquired over a manmade concrete tunnel located on the main campus of the University of Kansas (KU). Different workflows including FWI method and BSWI method are applied to the acquired data and tested for imaging the known tunnel. The field example demonstrates that BSWI can accurately image the tunnel. Compared with FWI, BSWI is less demanding in data processing. Finally, this thesis concludes that the proposed BSWI method is capable of efficiently detecting a near-surface tunnel with the minimum amount of data processing which lends it as a method suitable for application in the field.

Acknowledgements

Throughout the writing of this thesis I have received a great deal of support and assistance.

I would first like to especially thank Dr. Xuemin Tu for her guidance and mentoring in my study and research. She consistently allowed this thesis project to be my own work but steered me in the right direction whenever she though I needed it.

My sincere gratitude also goes to my committee members Dr. Georgios P. Tsoflias and Dr. Hongguo Xu for serving on the committee and providing helpful suggestions and edits throughout this research.

Thanks to Dr. Ming Wang who provided me fellowship opportunity as allowed me to work as a teaching assistant in her course MATH 365.

I would like to thank my tutors and colleague graduate students of the Department of Mathematics at University of Kansas. Without their passionate and patient teaching, grading, and advising, I would have never realized how amazing mathematics is. I would like to thank students of the Department of Geology at University of Kansas who have contributed their time and energy in acquisition of the seismic data used for this research project. And I am gratefully indebted to their valuable comments and constructive critiques made during discussions.

Finally, I would also like to express my gratitude with joy to my family: my wife Jingjin Yu and our parents for supporting me spiritually throughout my entire life.

Table of Contents

List of Figures

Chapter I: Introduction

A significant environmental and engineering geophysical task is to obtain accurate images of near-surface (upper 10-100 m) structures, such as tunnels, sinkholes, fractures, and faults. These structures give rise to seismic velocity anomalies which introduce disturbances, including reflections, refractions, and diffractions, to the propagating wavefield. The information contained in the wavefield disturbances, such as traveltime, magnitude, and polarity, can be used to resolve the subsurface velocity structure and the location of the velocity anomalies. Among all the disturbances in the seismic wavefield, the author considers back-scattered surface waves which are generated by seismic waves impinging on the velocity anomalies and diffracting back toward the source. These back-scattered events have less interference by other wave modes. In addition, the back-scattered surface waves can be easily distinguished in the frequency-wavenumber (F-k) domain. Xia et al. (2007) studied and demonstrated the feasibility of using the back-scattered surface waves to detect near-surface features. Therefore, the back-scattered surface waves are potential resources to efficiently resolve the spatial location and velocity structure of the anomalies.

In this research, the author developed a back-scattered surface wave waveform inversion (BSWI) method to detect near-surface tunnels. In this inversion method, the objective function is designed to be sensitive to the misfit of the back-scattered waveforms. The author tested the proposed method on numerical and field data and compared its performance with the conventional waveform inversion method. The results of this research have demonstrated the effectiveness and efficiency of the proposed method. Furthermore, because of the high signal-noise-ratio (SNR) of the back-scattered surface waves in the F-k domain, the BSWI requires less

effort in data processing. These features enable the BSWI to perform efficient in-situ tunnel detections.

To resolve near-surface velocity structures, the conventional seismic methods include reflection method, refraction method, surface wave method, and tomography method. The pure reflection and refraction methods image the subsurface velocity structures in the data domain. However, the necessary data processing steps required by these methods are time-consuming and usually demand experience in interpretation. Often, these two methods are combined with the surface wave methods and tomography methods when the subsurface velocity structure is complicated.

A conventional surface wave method is the multi-channel analysis of surface waves (MASW; Park et al., 1999). The conventional MASW method is a pseudo-2D approach that each shot produces a most-likely 1D shear wave velocity for the vertical transversely isotropic (VTI) model. Then, each 1D Vs profile is placed at a surface location corresponding to the midpoint of the receiver spread where a series of coincident shots are combined to produce a 2D profile (Park et al., 2007). Consequently, if the size of the anomaly is smaller than the separation between the two nearest midpoints or receivers, the image could be below the reasonable resolving level of the method. Despite the lateral resolution limitation of the method, surface waves are being widely used for near surface imaging because these methods are robust and adaptable to various geological conditions.

Tomography methods include travel-time tomography method and waveform tomography method. These tomography methods minimize the differences between observation and simulation of seismic waves in terms of travel-time or waveform. The travel-time tomography methods commonly use ray-theory (Jacob, 1970) or eikonal equation (Born M, 1964) to simulate

the seismic wave travel time between any pair of two nodes in velocity model. Meanwhile, the waveform tomography methods (Full-waveform inversion; Tarantola, 1984) are data-driven inversion approach of quantifying models of rock properties by iteratively minimizing the objective function constructed by the misfits between the observed and simulated waveforms. The tomography methods have improved the imaging resolution to the wavelength-level by utilizing wave equations during the imaging process. However, the tomography methods are demanding in signal processing. For the travel-time tomography, the travel times for the reflection or refraction events need to be picked from the seismograms. The time-picking process is relative easier if the area of interest is deep in the earth because the large travel time allows the wave modes with different velocities to separate. However, for near surface surveys, the incomplete separation in wave modes render the time-picking process difficult. For the waveform tomography, routine signal processing includes source signal estimation and noise attenuation. These signal processing steps are time-consuming and demanding, which prevents the conventional waveform tomography methods from becoming an efficient in-situ near surface imaging method.

The back-scattered waves are generated by seismic waves impinging on the velocity anomalies and diffracting back toward the source. This unique propagation mode results in that back-scattered waves containing less consistent noise. Among the back-scattered events, the back-scattered surface waves, which have large magnitudes and decay slowly with time and travel distance, are dominant in elastic energy. A classical digital signal processing method - frequency-wavenumber domain filtering - can drastically enhance the back-scattered waves. In the frequency-wavenumber (F-k) domain, the back-scattered surface waves are evident and can be used to determine the location of the velocity anomalies. In this research, the author

developed a new method for near surface velocity anomaly detection by using waveform inversion of the back-scattered surface waves. During the waveform inversion, the author designed an objective function which is sensitive to the back-scattered wavefield. With this changing of weight in the objective function, the proposed method is demonstrated to be efficient in near surface velocity anomaly detection.

This research includes numerical and field experiments. The numerical examples include a checkerboard-model test and a single-sinkhole-model test. These numerical examples are used to demonstrate the feasibility of the proposed method. Using a field seismic data acquired over an underground manmade concrete tunnel, the author researched the application of the new method in accurately seismic imaging the near surface. The tunnel is located on the main campus of University of Kansas (KU). The 2D seismic data were acquired by the Department of Geology of KU in 2014. This survey includes a fixed spread of forty-eight vertical-component 28 Hz geophones. This data set allows the author to test and study the tunnel imaging in the urban environment by using the proposed method. The successful outcomes of the numerical and field examples demonstrate the feasibility and efficiency of the proposed BSWI method in detecting near surface velocity anomalies.

Chapter II: Literature Review

Determining near surface seismic structures and detecting underground voids are important concerns for public safety. Therefore, various surface-wave-based seismic methods have been applied to investigate velocity structures on the top (10-100 m) region of the crust. Multi-channel analysis of surface waves (MASW; Park et al., 1999) has been used to study near surface shear-wave velocity structures for over two decades. Ivanov et al. (2013) applied joint analysis of refractions with surface waves (JARS) for profiling of surface wave and body wave structures. Sloan et al. (2010) used multiple seismic wave modes including diffracted body waves, back-scattered surface waves, and reflected waves for void detection. Livers et al. (2015) performed a parallel beamsteering method by using the F-k filtering to enhance tunnel image. In general application, Sloan et al. (2015) successfully detected a series of clandestine tunnels by using the P-wave diffraction method and surface-wave back-scatter technique.

Numerical and field studies have reported success in profiling subsurface velocity structures by using the full-waveform inversion (FWI; Tarantola, 1984; Mora, 1987). The resolution of FWI is defined by the scattering wavenumber, which is related to the frequency and diffraction angle (Virieux and Operto, 2009). In the past few decades, FWI has been widely used for solving near surface geological engineering problems. By taking advantage of high-energy surface waves, successful near-surface FWI applications have revealed the potential of FWI as an advanced seismic imaging method at the near-surface. Amrouche and Yamanaka (2014) studied shallow soil profiling using 2D FWI. Dou and Ajo-Franklin (2014) applied FWI of surface waves for mapping seismic structures in permafrost. Yuan et al. (2015) utilized a wavelet-multiscale adjoint scheme for the waveform inversion of seismic data including surface waves and body waves.

This research is also inspired by successful applications of FWI in the civil and environmental engineering. Chen et al. (2016) successfully applied a frequency-dependent traveltime tomography and the FWI on the P- and SH-wave refraction data to detect a known near-surface tunnel. Wang et al. (2018) and Smith et al. (2018) applied the 2D and 3D FWI to detect a 10-meter-deep hand-dug tunnel at the Yuma Proving Ground, Arizona. Tran and Sperry (2018) applied FWI with a land-streamer acquisition system to assess roadway subsidence. Sherman et al. (2018) determined the location of a manmade tunnel at the Black Diamond Mines, CA. These studies indicate that the application of FWI to near-surface narrow-aperture datasets has great potential in the near-surface engineering and environmental imaging tasks.

Chapter III: Methods

This chapter introduces the theoretical background of the proposed BSWI method and the geology background of the site of interest. The theory presented includes:

(1) Time domain finite difference solution to 2D elastic wave equations.

(2) Adjoint problem of 2D waveform inversion.

(3) Conjugate gradient optimization method.

(4) Frequency-wavenumber domain filtering.

Based on this background theory, the BSWI method is derived particularly to resolve the near-surface scatter detection problem.

Time domain Finite difference (FDTD) solution to elastic wave equations

In this part, the 3D elastic wave equation will be introduced in general and then the 2D elastic wave equations will be obtained automatically. In 3D space, let displacement vector $\vec{\delta}$ be

$$\vec{\delta}(x,y,z,t) = \begin{bmatrix} \delta^1(x,y,z,t) \\ \delta^2(x,y,z,t) \\ \delta^3(x,y,z,t) \end{bmatrix} = \begin{bmatrix} X(x,y,z,t) \\ Y(x,y,z,t) \\ Z(x,y,z,t) \end{bmatrix} - \begin{bmatrix} x \\ y \\ z \end{bmatrix}. \quad (1)$$

$\begin{bmatrix} X(x,y,z,t) \\ Y(x,y,z,t) \\ Z(x,y,z,t) \end{bmatrix}$ represents the location at time t, and $\begin{bmatrix} x \\ y \\ z \end{bmatrix}$ is the reference location. The velocity vector $\vec{u}$ is the time derivative of displacement vector

$$\vec{u}(x,y,z,t) = \begin{bmatrix} u(x,y,z,t) \\ v(x,y,z,t) \\ w(x,y,z,t) \end{bmatrix} = \begin{bmatrix} \delta_t^1(x,y,z,t) \\ \delta_t^2(x,y,z,t) \\ \delta_t^3(x,y,z,t) \end{bmatrix} \tag{2}$$

The displacement gradient $\nabla\vec{\delta}$ is the strain within body (ε) plus the rigid rotations (Ω):

$$\nabla\vec{\delta} = \varepsilon + \Omega = \begin{bmatrix} \delta_x^1 & \delta_y^1 & \delta_z^1 \\ \delta_x^2 & \delta_y^2 & \delta_y^2 \\ \delta_x^3 & \delta_y^3 & \delta_z^3 \end{bmatrix} = \begin{bmatrix} \delta_{xx} & \delta_{xy} & \delta_{xz} \\ \delta_{yx} & \delta_{yy} & \delta_{yz} \\ \delta_{zx} & \delta_{zy} & \delta_{zz} \end{bmatrix} = \begin{bmatrix} X_x - 1 & X_y & X_z \\ Y_x & Y_y - 1 & Y_z \\ Z_x & Z_y & Z_z - 1 \end{bmatrix}. \tag{3}$$

The strain matrix ε , which is symmetric, can be written as

$$\varepsilon = \frac{1}{2}\left[\nabla\vec{\delta} + \left(\nabla\vec{\delta}\right)^T\right] = \begin{bmatrix} \delta_x^1 & \frac{1}{2}\left(\delta_y^1 + \delta_x^2\right) & \frac{1}{2}(\delta_z^1 + \delta_x^3) \\ \frac{1}{2}\left(\delta_x^2 + \delta_y^1\right) & \delta_y^2 & \frac{1}{2}\left(\delta_z^2 + \delta_y^3\right) \\ \frac{1}{2}(\delta_x^3 + \delta_z^1) & \frac{1}{2}\left(\delta_y^3 + \delta_z^2\right) & \delta_z^3 \end{bmatrix} \tag{4}$$

$$= \begin{bmatrix} \varepsilon^{11} & \varepsilon^{12} & \varepsilon^{13} \\ \varepsilon^{21} & \varepsilon^{22} & \varepsilon^{23} \\ \varepsilon^{31} & \varepsilon^{32} & \varepsilon^{33} \end{bmatrix} = \begin{bmatrix} \varepsilon_{xx} & \varepsilon_{xy} & \varepsilon_{xz} \\ \varepsilon_{yx} & \varepsilon_{yy} & \varepsilon_{yz} \\ \varepsilon_{zx} & \varepsilon_{zy} & \varepsilon_{zz} \end{bmatrix}.$$

And the rotation matrix Ω, which is skew-symmetric, can be written as

$$\Omega = \frac{1}{2}\left[\nabla\vec{\delta} - \left(\nabla\vec{\delta}\right)^T\right]$$

$$= \begin{bmatrix} 0 & \frac{1}{2}\left(\delta_y^1 - \delta_x^2\right) & \frac{1}{2}(\delta_z^1 - \delta_x^3) \\ \frac{1}{2}\left(\delta_x^2 - \delta_y^1\right) & 0 & \frac{1}{2}\left(\delta_z^2 - \delta_y^3\right) \\ \frac{1}{2}(\delta_x^3 - \delta_z^1) & \frac{1}{2}\left(\delta_y^3 - \delta_z^2\right) & 0 \end{bmatrix} \quad (5)$$

Because of the velocity vector $\vec{u}$ is the time derivative of displacement vector $\vec{\delta}$, the following equations are describing the motion of an elastic body,

$$\begin{cases} \varepsilon_{\mathrm{t}}^{11} = \frac{\partial}{\partial t}\delta_x^1 = u_x \\ \varepsilon_{\mathrm{t}}^{22} = \frac{\partial}{\partial t}\delta_y^2 = v_y \\ \varepsilon_{\mathrm{t}}^{33} = \frac{\partial}{\partial t}\delta_z^3 = w_z \\ \varepsilon_{\mathrm{t}}^{12} = \frac{\partial}{\partial t}\left[\frac{1}{2}\left(\delta_y^1 + \delta_x^2\right)\right] = \frac{1}{2}\left(v_x + u_y\right) \\ \varepsilon_{\mathrm{t}}^{23} = \frac{\partial}{\partial t}\left[\frac{1}{2}\left(\delta_z^2 + \delta_y^3\right)\right] = \frac{1}{2}\left(v_z + w_y\right) \\ \varepsilon_{\mathrm{t}}^{31} = \frac{\partial}{\partial t}\left[\frac{1}{2}(\delta_x^3 + \delta_z^1)\right] = \frac{1}{2}(u_z + w_x) \end{cases}. \quad (6)$$

By using Newton's second law, the density ρ and the acceleration of a unit elastic body relate to the stress matrix (σ):

$$\rho\frac{\partial^2\delta_{\mathrm{j}}}{\partial \mathrm{t}^2} = \frac{\partial\sigma_{ij}}{\partial x_i},$$

$$\sigma = \begin{bmatrix} \sigma^{11} & \sigma^{12} & \sigma^{13} \\ \sigma^{21} & \sigma^{22} & \sigma^{23} \\ \sigma^{31} & \sigma^{32} & \sigma^{33} \end{bmatrix}.$$

The following equations can be derived by applying Newton's second law,

$$\begin{cases} \rho u_t - \sigma_x^{11} - \sigma_y^{12} - \sigma_z^{13} = 0, \\ \rho v_t - \sigma_x^{21} - \sigma_y^{22} - \sigma_z^{23} = 0, \\ \rho w_t - \sigma_x^{31} - \sigma_y^{32} - \sigma_z^{33} = 0. \end{cases} \tag{7}$$

By Hooke's law there is a linear relation between the strain and stress in an elastic body when the strain is no greater than then limit of proportionality:

$$\sigma = E * \varepsilon.$$

E is the Young's modulus which relates tensors of strain and stress. To connect the elements of the strain tensor, use the Poisson's ratio which is defined as

$$\gamma = \frac{lateral\ strain}{axial\ strain},$$

and hence there are

$$\varepsilon^{22} = \varepsilon^{33} = -\gamma\varepsilon^{11} = -\frac{\gamma}{E}\sigma^{11}. \tag{8}$$

Define the shear modulus as

$$\mu = \frac{E}{2(1+\gamma)},$$

then we have

$$\begin{cases} \sigma^{12} = 2\mu\varepsilon^{12}, \\ \sigma^{13} = 2\mu\varepsilon^{13}, \\ \sigma^{23} = 2\mu\varepsilon^{23}, \\ \varepsilon^{11} = \frac{1}{E}\sigma^{11} - \frac{\gamma}{E}\sigma^{22} - \frac{\gamma}{E}\sigma^{33}, \\ \varepsilon^{22} = \frac{1}{E}\sigma^{22} - \frac{\gamma}{E}\sigma^{11} - \frac{\gamma}{E}\sigma^{22}, \\ \varepsilon^{33} = \frac{1}{E}\sigma^{33} - \frac{\gamma}{E}\sigma^{11} - \frac{\gamma}{E}\sigma^{22}. \end{cases} \tag{9}$$

To simplify equations (9) in matrix form, we have

$$\begin{bmatrix} \varepsilon^{11} \\ \varepsilon^{22} \\ \varepsilon^{33} \\ \varepsilon^{12} \\ \varepsilon^{23} \\ \varepsilon^{31} \end{bmatrix} = \begin{bmatrix} \frac{1}{E} & -\frac{\gamma}{E} & -\frac{\gamma}{E} & 0 & 0 & 0 \\ -\frac{\gamma}{E} & \frac{1}{E} & -\frac{\gamma}{E} & 0 & 0 & 0 \\ -\frac{\gamma}{E} & -\frac{\gamma}{E} & \frac{1}{E} & 0 & 0 & 0 \\ 0 & 0 & 0 & \frac{1}{2\mu} & 0 & 0 \\ 0 & 0 & 0 & 0 & \frac{1}{2\mu} & 0 \\ 0 & 0 & 0 & 0 & 0 & \frac{1}{2\mu} \end{bmatrix} \begin{bmatrix} \sigma^{11} \\ \sigma^{22} \\ \sigma^{33} \\ \sigma^{12} \\ \sigma^{23} \\ \sigma^{31} \end{bmatrix}. \tag{10}$$

With the introduction of Lamé parameters λ and μ,

$$\lambda = \frac{\gamma E}{(1+\gamma)(1-2\gamma)},$$

$$\mu = \frac{E}{2(1+\gamma)},$$

the equations of stress matrix in terms of strain matrix becomes

$$\begin{bmatrix} \sigma^{11} \\ \sigma^{22} \\ \sigma^{33} \\ \sigma^{12} \\ \sigma^{23} \\ \sigma^{31} \end{bmatrix} = \begin{bmatrix} \lambda + 2\mu & \lambda & \lambda & 0 & 0 & 0 \\ \lambda & \lambda + 2\mu & \lambda & 0 & 0 & 0 \\ \lambda & \lambda & \lambda + 2\mu & 0 & 0 & 0 \\ 0 & 0 & 0 & 2\mu & 0 & 0 \\ 0 & 0 & 0 & 0 & 2\mu & 0 \\ 0 & 0 & 0 & 0 & 0 & 2\mu \end{bmatrix} \begin{bmatrix} \varepsilon^{11} \\ \varepsilon^{22} \\ \varepsilon^{33} \\ \varepsilon^{12} \\ \varepsilon^{23} \\ \varepsilon^{31} \end{bmatrix}, \tag{11}$$

equation (14) can be written in terms of stress tensor σ_{ij} and strain tensor ε_{kl}

$$\sigma_{ij} = c_{ijkl}\varepsilon_{kl}. \tag{12}$$

In this expression (12), c_{ijkl} are the components of the fourth-order stiffness tensor of elastic moduli. The fourth-order stiffness tensor has 81 and 16 components for 3D and 2D problems,

respectively. Derivate (11) with respect to time t and together with equation (7), we have the following equations

$$\begin{cases} \sigma_t^{11} - (\lambda + 2\mu)u_x - \lambda v_y - \lambda w_z = 0, \\ \sigma_t^{22} - \lambda u_x - (\lambda + 2\mu)v_y - \lambda w_z = 0, \\ \sigma_t^{33} - \lambda u_x - \lambda v_y - (\lambda + 2\mu)w_z = 0, \\ \sigma_t^{12} - \mu\left(v_x + u_y\right) = 0, \\ \sigma_t^{23} - \mu\left(v_z + w_y\right) = 0, \\ \sigma_t^{13} - \mu(u_z + w_x) = 0, \\ \rho u_t - \sigma_x^{11} - \sigma_y^{12} - \sigma_z^{13} = 0, \\ \rho v_t - \sigma_x^{21} - \sigma_y^{22} - \sigma_z^{23} = 0, \\ \rho w_t - \sigma_x^{31} - \sigma_y^{32} - \sigma_z^{33} = 0. \end{cases} \tag{13}$$

In 2D (x-y plane), these equations reduce to

$$\begin{cases} \sigma_t^{11} - (\lambda + 2\mu)u_x - \lambda v_y = 0, \\ \sigma_t^{22} - \lambda u_x - (\lambda + 2\mu)v_y = 0, \\ \sigma_t^{12} - \mu\left(v_x + u_y\right) = 0, \\ \sigma_t^{21} - \mu\left(v_y + u_x\right) = 0, \\ \rho u_t - \sigma_x^{11} - \sigma_y^{12} = 0, \\ \rho v_t - \sigma_x^{21} - \sigma_y^{22} = 0. \end{cases} \tag{14}$$

In this research, the author utilized a time domain finite difference (FDTD) method to calculate the numerical solution to the 2D elastic wave equations. For each time step, the utilized finite difference method updates first the stress tensor then the velocity vector. The finite difference scheme used in this research is a staggered scheme (Levander, 1988; Virieux, 1986) which does not place the variables on the same grid points when calculating the spatial derivatives. To specify, the utilized FD scheme can be explicitly written as

$$\begin{cases} \mu_{xy}\left[j+\frac{1}{2}\right]\left[i+\frac{1}{2}\right] = \left[\frac{1}{4}(\mu^{-1}[j][i]+\mu^{-1}[j][i+1]+\mu^{-1}[j+1][i+1]+\mu^{-1}[j+1][i])\right]^{-1}, \\ \rho_x[j]\left[i+\frac{1}{2}\right] = \frac{1}{2}(\rho[j][i+1]+\rho[j][i]), \\ \rho_x\left[j+\frac{1}{2}\right][i] = \frac{1}{2}(\rho[j+1][i]+\rho[j][i]). \end{cases} \tag{15}$$

To update the stress matrix, there are equations

$$\begin{cases} u_x[j][i] \approx \frac{u[j]\left[i+\frac{1}{2}\right]-u[j]\left[i-\frac{1}{2}\right]}{dh}, \\ v_y[j][i] \approx \frac{v\left[j+\frac{1}{2}\right][i]-v\left[j-\frac{1}{2}\right][i]}{dh}, \\ u_y\left[j+\frac{1}{2}\right]\left[i+\frac{1}{2}\right] \approx \frac{u[j+1]\left[i+\frac{1}{2}\right]-u[j]\left[i+\frac{1}{2}\right]}{dh}, \\ v_x\left[j+\frac{1}{2}\right]\left[i+\frac{1}{2}\right] \approx \frac{v\left[j+\frac{1}{2}\right][i+1]-v\left[j+\frac{1}{2}\right][i]}{dh}, \\ \sigma_{n+1}^{11}[j][i] \approx \sigma_n^{11}[j][i] + dt\cdot\lambda[j][i]\cdot\left(u_x[j][i]+v_y[j][i]\right)+2dt\cdot\mu_{xy}[j][i]\cdot u_x[j][i], \\ \sigma_{n+1}^{22}[j][i] \approx \sigma_n^{22}[j][i] + dt\cdot\lambda[j][i]\cdot\left(u_x[j][i]+v_y[j][i]\right)+2dt\cdot\mu_{xy}[j][i]\cdot v_y[j][i], \\ \sigma_{n+1}^{12}\left[j+\frac{1}{2}\right]\left[i+\frac{1}{2}\right] \approx \sigma_n^{12}\left[j+\frac{1}{2}\right]\left[i+\frac{1}{2}\right] + dt\cdot\mu\left[j+\frac{1}{2}\right]\left[i+\frac{1}{2}\right]\cdot\left(u_y\left[j+\frac{1}{2}\right]\left[i+\frac{1}{2}\right]+v_x\left[j+\frac{1}{2}\right]\left[i+\frac{1}{2}\right]\right). \end{cases} \tag{16}$$

And to update the velocity vector, there are equations

$$\begin{cases} u_{tt}^n[j]\left[i+\frac{1}{2}\right] \approx \sigma^{11}[j][i+1]-\sigma^{11}[j][i]+\sigma^{12}\left[j+\frac{1}{2}\right][i]-\sigma^{12}\left[j-\frac{1}{2}\right][i], \\ v_{tt}^n[j]\left[i+\frac{1}{2}\right] \approx \sigma^{12}[j]\left[i+\frac{1}{2}\right]-\sigma^{12}[j]\left[i-\frac{1}{2}\right]+\sigma^{22}[j+1][i]-\sigma^{22}[j][i], \\ u_{n+1}[j]\left[i+\frac{1}{2}\right] \approx u_n[j]\left[i+\frac{1}{2}\right]+\frac{dt}{dh\cdot\rho_x[j]\left[i+\frac{1}{2}\right]}\cdot u_{tt}^n[j]\left[i+\frac{1}{2}\right], \\ v_{n+1}\left[j+\frac{1}{2}\right][i] \approx v_n\left[j+\frac{1}{2}\right][i]+\frac{dt}{dh\cdot\rho_y\left[j+\frac{1}{2}\right][i]}\cdot v_{tt}^n\left[j+\frac{1}{2}\right][i]. \end{cases} \tag{17}$$

For boundary treatment, an unsplit convolutional perfectly matched layer (PML) absorbing boundary condition (Komatitsch & Martin, 2007) is applied to reduce the reflection from the boundaries.

Adjoint problem of 2D waveform inversion.

The misfit in 2D data $\boldsymbol{u} = \left[u_x, u_y\right]^{\mathrm{T}}$ can be measured by a vector norm $|L|_{\mathrm{p}}$ which is defined for p=1, 2, …, ∞ as

$$|L|_{\mathrm{p}} = \left[\int dt|\delta\boldsymbol{u}(t)|^p\right]^{\frac{1}{p}}$$

$$= \left(\sum_{i=0}^{nt}|\delta\boldsymbol{u}_i|^p\right)^{1/p}.$$

$$\delta\boldsymbol{u} = \boldsymbol{u}^{syn} - \boldsymbol{u}^{obs}.$$

Especially, the L2-norm

$$\begin{aligned} \mathrm{E} &= |L|_2 \\ &= \frac{1}{2}\delta\boldsymbol{u}^T\delta\boldsymbol{u} \\ &= \frac{1}{2}\sum_{sources}\int dt\sum_{receivers}\delta u^2(\overrightarrow{x_s},\overrightarrow{x_r},t). \end{aligned} \tag{18}$$

$\delta u(\overrightarrow{x_s},\overrightarrow{x_r},t)$ is the data residual at station $(\overrightarrow{x_s},\overrightarrow{x_r})$ at time t.

Derivate (18) with respect to the model parameter m we get

$$\begin{aligned} \frac{\partial E}{\partial m} &= \sum_{sources}\int dt\sum_{receivers}\frac{\partial\delta\boldsymbol{u}_{r,s}}{\partial m}\delta\boldsymbol{u} \\ &= \sum_{sources}\int dt\sum_{receivers}\frac{\partial(\boldsymbol{u}_{r,s}^{syn}(m)-\boldsymbol{u}_{r,s}^{obs})}{\partial m}\delta\boldsymbol{u} \\ &= \sum_{sources}\int dt\sum_{receivers}\frac{\partial\boldsymbol{u}_{r,s}^{syn}(m)}{\partial m}\delta\boldsymbol{u}. \end{aligned} \tag{19}$$

Next, we consider the mapping between model space and data space. If the Frechét derivative $\frac{\partial u}{\partial m}$ is known, a small perturbation of data space $\delta\hat{u}$ can be represented by an integral of all small perturbation in model space δm over the model volume Ω

$$\delta\hat{u} = \int_{\Omega} d\omega \frac{\partial u}{\partial m} \delta m. \tag{20}$$

And similarly, small changes in the data space $\delta u'$ can be integrated to calculate the change in the model space $\delta \mathrm{m}'$

$$\begin{aligned} \delta \mathrm{m}' &= \int_{\Omega} d\omega \left[\frac{\partial u}{\partial m}\right]^{*} \delta\hat{u}' \\ &= \sum_{sources} \int dt \sum_{receivers} \left[\frac{\partial u_{r,s}}{\partial m}\right]^{*} \delta\hat{u}'. \end{aligned} \tag{21}$$

The asterisk sign denotes the conjugate transpose. We introduce linear operators

$$\delta\hat{u} = \hat{L}\delta m = \int_{\Omega} d\omega \frac{\partial u}{\partial m} \delta m, \tag{22}$$

$$\delta \mathrm{m}' = \hat{L}^{*}\delta\hat{u}' = \int_{\Omega} d\omega \left[\frac{\partial u}{\partial m}\right]^{*} \delta\hat{u}'. \tag{23}$$

It has been shown that for seismic wave tomography problem, the kernels of $\hat{L}$ and its adjoint counterpart are identical (Chapter 5.4.2, Tarantola, 2005)

$$\left[\frac{\partial u}{\partial m}\right]^{*} = [\frac{\partial u}{\partial m}]. \tag{24}$$

Then, we substitute $\frac{\partial u}{\partial m}$ with $\left[\frac{\partial u}{\partial m}\right]^{*}$ in equation (21) to find that small model space perturbation $\delta \mathrm{m}'$ can be calculated with $\frac{\partial E}{\partial m}$ which is defined in equation (19)

$$
\begin{aligned}
\delta \mathrm{m}' &= \int_{\Omega} d\omega \left[\frac{\partial u}{\partial m}\right]^{*} \delta \hat{u}' \\
&= \sum_{sources} \int dt \sum_{receivers} \left[\frac{\partial u_{r,s}}{\partial m}\right]^{*} \delta \hat{u}' \\
&= \sum_{sources} \int dt \sum_{receivers} \frac{\partial u_{r,s}}{\partial m} \delta \hat{u}' \\
&= \frac{\partial \mathrm{E}}{\partial \mathrm{m}}.
\end{aligned}
\tag{25}
$$

Apply this adjoint method to 2D elastic wavefield inverse problem. Adjust the 2D elastic wave equations (12) and (14) by introducing source terms, we obtain equations

$$
\sigma_{\mathrm{ij}} - c_{ijkl}\varepsilon_{\mathrm{kl}} = T_{ij}. \tag{26}
$$

$$
\begin{cases}
\varepsilon_{xy} = \dfrac{1}{2}\left(\dfrac{\partial u_x}{\partial y} + \dfrac{\partial u_y}{\partial x}\right), \\
\varepsilon_{\mathrm{yx}} = \dfrac{1}{2}\left(\dfrac{\partial u_y}{\partial x} + \dfrac{\partial u_x}{\partial y}\right), \\
\rho \dfrac{\partial^2 u_x}{\partial \mathrm{t}^2} - \dfrac{\partial \sigma^{11}}{\partial x} - \dfrac{\partial \sigma^{12}}{\partial y} = f_x(t), \\
\rho \dfrac{\partial^2 u_y}{\partial \mathrm{t}^2} - \dfrac{\partial \sigma^{21}}{\partial x} - \dfrac{\partial \sigma^{22}}{\partial y} = f_y(t).
\end{cases}
\tag{27}
$$

In equations (26) and (27), f_x, f_y, and $\mathrm{T_{ij}}$ are source terms for volume in x- and y-direction and surface forces, respectively. With small perturbations in every parameter

$$
\begin{cases}
u_{\mathrm{i}} \to u_i + \delta u_i, \\
\rho \to \rho + \delta\rho, \\
\sigma_{ij} \to \sigma_{ij} + \delta\sigma_{ij}, \\
c_{ijkl} \to c_{ijkl} + \delta c_{ijkl}, \\
\varepsilon_{\mathrm{ij}} \to \varepsilon_{\mathrm{ij}} + \delta\varepsilon_{\mathrm{ij}},
\end{cases}
\tag{28}
$$

equation (26) and (27) become

$$\delta\sigma_{\mathrm{ij}} - c_{ijkl}\delta\varepsilon_{\mathrm{kl}} = \Delta T_{ij}. \tag{29}$$

$$\begin{cases} \delta\varepsilon_{xy} = \delta\varepsilon_{yx} = \dfrac{1}{2}\left(\dfrac{\partial\delta u_y}{\partial x} + \dfrac{\partial\delta u_x}{\partial y}\right), \\ \rho\dfrac{\partial^2\delta u_x}{\partial \mathrm{t}^2} - \dfrac{\partial\delta\sigma^{11}}{\partial x} - \dfrac{\partial\delta\sigma^{12}}{\partial y} = \Delta f_x(t), \\ \rho\dfrac{\partial^2\delta u_y}{\partial \mathrm{t}^2} - \dfrac{\partial\delta\sigma^{21}}{\partial x} - \dfrac{\partial\delta\sigma^{22}}{\partial y} = \Delta f_y(t). \end{cases} \tag{30}$$

The new source terms are

$$\begin{cases} \Delta f_i = -\delta\rho\dfrac{\partial^2 u_i}{\partial \mathrm{t}^2}, \\ \Delta T_{ij} = \delta c_{ijkl}\varepsilon_{\mathrm{kl}}. \end{cases} \tag{31}$$

We note that equations (29) and (30) are similar in form to equations (26) and (27) because the medium parameters c_{ijkl} and ρ are unchanged in these equations. Equations (29) and (30) state that small perturbations in parameters (28) are equivalent to virtual sources (31) of the perturbed wavefield, and that the perturbed wavefield is propagating in the medium without perturbations. Therefore, the solution to the new elastic wave equations (29) and (30) can be obtained in terms of Green's function $\mathrm{G_{ij}}(x, t; x', t')$. Consider the perturbed wavefield

$$\begin{aligned} \delta u_i(x,t) = &\int_\Omega d\omega \int_0^T dt' G_{ij}(x,t;x',t')\Delta f_j(x',t') \\ &- \int_\Omega d\omega \int_0^T dt' \frac{\partial G_{ij}}{\partial x_k'}(x,t;x',t')\Delta T_{jk}(x',t'). \end{aligned} \tag{32}$$

Substituting the new source terms (31) into equation (32) to obtain

$$\delta u_i(x,t) = -\int_\Omega d\omega \int_0^T dt' G_{ij}(x,t;x',t') \frac{\partial^2 u_j}{\partial \mathrm{t}^2}(x',t')\delta\rho - \int_\Omega d\omega \int_0^T dt' \frac{\partial G_{ij}}{\partial x'_k}(x,t;x',t')\varepsilon_{lm}(x',t')\delta c_{jklm}. \tag{33}$$

Considering medium isotropy in equation (33) yields the Born approximation (Gubernatis et al., 1977; Hudson et al., 1981)

$$\begin{aligned}\delta u_i(x,t) = &-\int_\Omega d\omega \int_0^T dt' G_{ij}(x,t;x',t') \frac{\partial^2 u_j}{\partial \mathrm{t}^2}(x',t')\delta\rho \\ &- \int_\Omega d\omega \int_0^T \left[dt' \frac{\partial G_{ij}}{\partial x'_k}(x,t;x',t')\varepsilon_{lm}(x',t')\delta_{jk}\delta_{lm}\right]\delta\lambda \\ &- \int_\Omega d\omega \int_0^T \left[dt' \frac{\partial G_{ij}}{\partial x'_k}(x,t;x',t')\varepsilon_{lm}(x',t')(\delta_{jl}\delta_{lm} + \delta_{jm}\delta_{kl})\right]\delta\mu.\end{aligned} \tag{34}$$

Equation (34) has the same form as equation (22). Therefore, Frechét derivatives for the individual parameters ρ, λ, μ are

$$\begin{cases} \dfrac{\partial \mathrm{u_i}}{\partial \rho} = \displaystyle\int_0^T dt' G_{ij}(x,t;x',t') \frac{\partial^2 u_j}{\partial \mathrm{t}^2}(x',t'), \\ \dfrac{\partial \mathrm{u_i}}{\partial \lambda} = \displaystyle\int_0^T dt' \frac{\partial G_{ij}}{\partial x'_k}(x,t;x',t')\varepsilon_{lm}(x',t')\delta_{jk}\delta_{lm}, \\ \dfrac{\partial \mathrm{u_i}}{\partial \mu} = \displaystyle\int_0^T dt' \frac{\partial G_{ij}}{\partial x'_k}(x,t;x',t')\varepsilon_{lm}(x',t')(\delta_{jl}\delta_{lm} + \delta_{jm}\delta_{kl}). \end{cases} \tag{35}$$

By definition (21), the adjoint operator can be written as

$$\delta \mathrm{m}' = \sum_{sources} \int dt \sum_{receivers} \left[\frac{\partial u_i}{\partial m}\right]^* \delta u'_i(x_{receiver}, t'). \tag{36}$$

Take conjugate transpose of each equation in (35) and then insert in (36) to obtain

$$\begin{cases} \delta\rho' = -\sum\limits_{sources}\int_0^T dt\left[\sum\limits_{receiver}\int_0^T dt' G_{ij}(x_{receiver},t';x,t)\dfrac{\partial^2 u_j}{\partial t^2}(x,t)\,\delta u_i'(x_{receiver},t')\right], \\ \delta\lambda' = -\sum\limits_{sources}\int_0^T dt\left[\sum\limits_{receiver}\int_0^T dt' \dfrac{\partial G_{ij}}{\partial x_k}(x_{receiver},t';x,t)\varepsilon_{lm}(x,t)\delta_{jk}\delta_{lm}\,\delta u_i'(x_{receiver},t')\right], \\ \delta\mu' = -\sum\limits_{sources}\int_0^T dt\left[\sum\limits_{receiver}\int_0^T dt' \dfrac{\partial G_{ij}}{\partial x_k}(x_{receiver},t';x,t)\varepsilon_{lm}(x,t)(\delta_{jl}\delta_{lm}+\delta_{jm}\delta_{kl})\,\delta u_i'(x_{receiver},t')\right]. \end{cases} \tag{37}$$

Define the wavefield

$$\Psi_j(x,t) = \sum_{receiver}\int_0^T dt' G_{ij}(x_{receiver},t';x,t)\,\delta u_i'(x_{receiver},t'),$$

and insert it to equations (37) to obtain

$$\begin{cases} \delta\rho' = -\sum\limits_{sources}\int_0^T dt\left[\dfrac{\partial^2 u_j}{\partial t^2}(x,t)\Psi_j\right], \\ \delta\lambda' = -\sum\limits_{sources}\int_0^T dt\left[\varepsilon_{lm}(x,t)\delta_{jk}\delta_{lm}\dfrac{\partial\Psi_j}{\partial x_k}\right], \\ \delta\mu' = -\sum\limits_{sources}\int_0^T dt\left[\varepsilon_{lm}(x,t)(\delta_{jl}\delta_{lm}+\delta_{jm}\delta_{kl})\dfrac{\partial\Psi_j}{\partial x_k}\right]. \end{cases} \tag{38}$$

For density ρ

$$\begin{aligned} \delta\rho' &= -\sum_{sources}\int_0^T dt\left[\frac{\partial^2 u_j}{\partial t^2}(x,t)\right]\Psi_j(x,t) \\ &= -\sum_{sources}\left\{\left[\frac{\partial u_j}{\partial t}(x,T)\Psi_j(x,T)\right]_0^T - \int_0^T dt\,\frac{\partial u_j}{\partial t}(x,t)\,\frac{\partial\Psi_j}{\partial t}(x,t)\right\}. \end{aligned} \tag{39}$$

Use the initial condition

$$\begin{cases} u_j(x,0) = 0, \\ \dfrac{\partial u_j}{\partial t}(x,0) = 0. \end{cases}$$

Therefore,

$$\delta\rho' = \sum_{sources} \int_0^T dt \frac{\partial u_j}{\partial \mathrm{t}}(x,t) \frac{\partial \Psi_j}{\partial \mathrm{t}}(x,t). \tag{40}$$

For parameters λ and μ, write out the implicit sums in (38) to get

$$\begin{cases} \delta\lambda' = -\sum_{sources} \int_0^T dt \left[\sum_l \sum_k \sum_j \sum_m \varepsilon_{lm}(x,t) \delta_{jk} \delta_{lm} \frac{\partial \Psi_j}{\partial x_k} \right], \\ \delta\mu' = -\sum_{sources} \int_0^T dt \left[\sum_l \sum_k \sum_j \sum_m \varepsilon_{lm}(x,t) (\delta_{jl}\delta_{lm} + \delta_{jm}\delta_{kl}) \frac{\partial \Psi_j}{\partial x_k} \right]. \end{cases} \tag{41}$$

For 2D problem, all wavefield components and derivatives in z-direction can be neglected to yield

$$\begin{cases} \delta\lambda' = -\sum_{sourcecs} \int_0^T dt (\varepsilon^{11} + \varepsilon^{22}) \left(\frac{\partial \Psi_x}{\partial x} + \frac{\partial \Psi_y}{\partial y} \right), \\ \delta\mu' = -\sum_{sourcecs} \int_0^T dt \left[(\varepsilon^{12} + \varepsilon^{21}) \left(\frac{\partial \Psi_x}{\partial y} + \frac{\partial \Psi_y}{\partial x} \right) \right] + 2 \left(\varepsilon^{11} \frac{\partial \Psi_x}{\partial x} + \varepsilon^{22} \frac{\partial \Psi_y}{\partial y} \right). \end{cases} \tag{42}$$

Use the definition of the strain tensor ϵ^{ij} and its relationship with displacement vector (4), we get

$$\begin{cases} \delta\lambda' = -\sum_{sourcecs} \int_0^T dt \left(\delta_x^1 + \delta_y^2\right) \left(\frac{\partial \Psi_x}{\partial x} + \frac{\partial \Psi_y}{\partial y} \right), \\ \delta\mu' = -\sum_{sourcecs} \int_0^T dt \left[\left(\delta_y^1 + \delta_x^2\right) \left(\frac{\partial \Psi_x}{\partial y} + \frac{\partial \Psi_y}{\partial x} \right) \right] + 2 \left(\delta_x^1 \frac{\partial \Psi_x}{\partial x} + \delta_y^2 \frac{\partial \Psi_y}{\partial y} \right). \end{cases} \tag{43}$$

Finally, the gradients for the Lamé parameters λ, μ, and the density ρ can be written as

$$\begin{cases} \delta\lambda' = -\sum_{sourcecs} \int_0^T dt \left(\delta_x^1 + \delta_y^2\right) \left(\frac{\partial \Psi_x}{\partial x} + \frac{\partial \Psi_y}{\partial y} \right), \\ \delta\mu' = -\sum_{sourcecs} \int_0^T dt \left[\left(\delta_y^1 + \delta_x^2\right) \left(\frac{\partial \Psi_x}{\partial y} + \frac{\partial \Psi_y}{\partial x} \right) \right] + 2 \left(\delta_x^1 \frac{\partial \Psi_x}{\partial x} + \delta_y^2 \frac{\partial \Psi_y}{\partial y} \right), \\ \delta\rho' = -\sum_{sourcecs} \int_0^T dt \left(\frac{\partial \delta^1}{\partial t} \frac{\partial \Psi_x}{\partial t} + \frac{\partial \delta^2}{\partial t} \frac{\partial \Psi_y}{\partial t} \right). \end{cases} \tag{44}$$

Use derivation from Shipp and Singh (2002), the displacement vector δ in equation (44) can be replaced by stresses σ, Σ and particle velocities u, v

$$\begin{cases} \delta\lambda = -\sum_{sources}\int dt\left[\dfrac{(\sigma_{xx}+\sigma_{zz})(\Sigma_{xx}+\Sigma_{zz})}{4(\lambda+\mu)^2}\right], \\ \delta\mu = -\sum_{sources}\int dt\left[\dfrac{\sigma_{xz}\Sigma_{xz}}{\mu^2}+\dfrac{1}{4}\left(\dfrac{(\sigma_{xx}+\sigma_{zz})(\Sigma_{xx}+\Sigma_{zz})}{(\lambda+\mu)^2}+\dfrac{(\sigma_{xx}-\sigma_{zz})(\Sigma_{xx}-\Sigma_{zz})}{\mu^2}\right)\right], \\ \delta\rho = -\sum_{sources}\int dt\left(\dfrac{\partial u}{\partial t}\Psi_x+\dfrac{\partial v}{\partial t}\Psi_y\right). \end{cases} \quad (45)$$

Where σ_{ij} and Σ_{ij} are the stresses of the forward- and backward-propagated wavefield, respectively. Displacements Ψ_i in the density gradient are calculated from the particle velocities using numerical integration.

Using the relationships between compressional-wave velocity (Vp), shear-wave velocity (Vs), Lamé parameters λ, μ, and the density ρ:

$$Vp = \sqrt{\frac{\lambda+2\mu}{\rho}}, Vs = \sqrt{\frac{\mu}{\rho}}, \qquad \lambda = \rho \mathrm{Vp}^2 - 2\rho Vs^2, \mu = \rho Vs^2, \quad (46)$$

the gradients in terms of Vp, Vs, and ρ can be written as

$$\begin{cases} \delta Vp = 2\rho Vp\delta\lambda, \\ \delta Vs = -4\rho Vs\delta\lambda + 2\rho Vs\delta\mu, \\ \delta\rho = (Vp^2 - 2Vs^2)\delta\lambda + Vs^2\delta\mu + \delta\rho. \end{cases} \quad (47)$$

Explicitly, the steepest descent direction of L2 misfit in terms of density and elastic velocities is obtained as equations (46) and (47) and therefore geological models can be updated by

$$\begin{cases} \mathrm{V_p^{n+1}} = \mathrm{V_p^n} + \theta_p^n \delta V_p^n, \\ \mathrm{V_s^{n+1}} = \mathrm{V_s^n} + \theta_s^n \delta V_s^n, \\ \mathrm{\rho^{n+1}} = \mathrm{\rho^n} + \theta_\rho^n \delta \mathrm{\rho^n}. \end{cases} \tag{48}$$

In equation (48), step lengths θ_p, θ_s, and θ_ρ are calculated by a parabolic line search method (Nocedal & Wright, 1999; Sourbier et al., 2009b, 2009a).

Conjugate gradient optimization method.

During the first iteration, the model is updated along the steepest descent direction $\delta\boldsymbol{m}$.

$$\boldsymbol{m}_2 = \boldsymbol{m}_1 + \theta^1 \delta \boldsymbol{m}_1. \tag{49}$$

To increase rate of convergence, a model is updated along conjugate direction δc for all successive iterations after the first iteration. Since $\delta\mathbf{c}_1 = \delta\boldsymbol{m}_1$, the conjugate direction at the n-th (n>1) iteration $\delta \mathrm{c_n}$ is calculated recursively by

$$\begin{cases} \delta \boldsymbol{c}_n = \delta \boldsymbol{m}_n + \beta^n \delta \boldsymbol{c}_{n-1}, \\ \boldsymbol{m}_{n+1} = \boldsymbol{m}_n + \theta^n \delta \boldsymbol{c}_n. \end{cases} \tag{50}$$

Conjugate gradient step length θ is estimated by parabolic line search method. The weighting factor β^{n} is calculated by Polak-Ribière method (Klessig & Polak, 1972)

$$\beta_{PR}^{\mathrm{n}} = \frac{\delta \boldsymbol{m}_n^T (\delta \boldsymbol{m}_n - \delta \boldsymbol{m}_{n-1})}{\delta \boldsymbol{m}_{n-1}^T \delta \boldsymbol{m}_{n-1})}.$$

Any negative weighting factor is reset to zero

$$\beta^{\mathrm{n}} = \max(0, \beta_{PR}^n)$$

to reset the search direction to be the steepest descent direction when subsequent search direction loses conjugacy.

In general, the implementation steps of a 2D waveform inversion procedure are as follow

(1) Data pre-processing to obtain u_{obs}. Pre-processing includes filter the observed seismic data to attenuate high-frequency random noises and consistent noises. Then eliminate low-SNR traces of each record to maintain stability of wavefield simulation process.

(2) Use time domain finite difference (FDTD) solver of 2D elastic wave equations with a model $\boldsymbol{m}$ to calculate the forward-propagating wavefield. Obtain synthetic seismic records u_{syn} and calculate data residual $\delta u = u_{syn} - u_{obs}$.

(3) Calculate the value of objective function $\mathrm{E}(\mathbf{m})$ with the chosen norm. For example, use equation (18) to calculate misfit using the L2 norm.

(4) Calculate steepest descent direction $\delta\boldsymbol{m}$ of the objective function by the virtual source method. For the first iteration, use $\delta\mathbf{c}_1 = \delta\boldsymbol{m}_1$. Starting from the second iteration, calculate conjugate gradient direction $\delta\mathbf{c}_\mathrm{n}$.

(5) Estimate step length θ^n for model updating with parabolic line search method.

(6) Update the model with $\boldsymbol{m}_{n+1} = \boldsymbol{m}_n + \theta^n \delta\boldsymbol{c}_\boldsymbol{n}$.

Site background and Data acquisition

To utilize the waveform inversion for tunnel detection, a seismic survey was conducted and 2D seismic data were acquired. In 2014, the KU Department of Geology collected a 2D seismic profile over a manmade concrete tunnel in the main campus of the University of Kansas. The underground tunnel connects the KU Union and the Spenser Museum of Art across Mississippi Street (Figure 1). The geology of the test site consists of consolidated dry soil and manmade

infrastructures including sidewalk, tunnel base and walls, and metal pipelines. The 2D seismic survey (Figure 1) includes a fixed spread of forty-eight stations and is approximately perpendicular to the tunnel. The survey line was northbound with its first station located at 0 m and its last station located at 70.5 m. With the source signals generated by a sledgehammer, the data were recorded by a group of single-component (vertical) 28 Hz geophones with a receiver station spacing of 1.5 m. Geophones were planted to the ground with spikes from station #1 to #21 and from station #31 to #48. From stations #22 (31.5 m) to #30 (45 m), the geophones were equipped with metal base plates and placed on the concrete sidewalk (Figure 2). Trace-by-trace data amplitude normalization was applied to the collected data. The normalization method used is defined as

$$\boldsymbol{d}_{\text{norm}} = \frac{\boldsymbol{d}}{\|\boldsymbol{d}\|_{L_\infty}}.$$

After normalization, no difference was distinguished between data collected on soil with spikes and data collected with baseplates.

The seismic survey contains nine shots located from 0 m to 80 m with a 10 m source interval. The geometry of the record system for each shot with reference to the first station (0 m) and the tunnel is displayed in Figure 3. The source signal for each shot is estimated from the trace with the minimum source-to-receiver offset (pilot trace). The source signals (Figure 4a) and their frequency spectra (Figure 4b) show that the source signals have a frequency range from 20 Hz to 60 Hz. For the signal processing, a frequency filter with a high-cut of 60 Hz can be applied to the data to reduce the influence of high-frequency random noise. The tunnel is located between 40 m and 45 m to the north of the first station. Figure 5a displays the interior of the tunnel beneath the seismic survey line, and Figure 5b shows the interior of the tunnel beneath Mississippi St. The

tunnel's interior dimensions are 4 m wide by 2.5 m high. The approximate depth from ground surface to the tunnel's roof and floor are 1.5 m and 4 m, respectively.

The nine records of the acquired seismic data are displayed in Figure 6a. From the seismograms, it can be observed that the raw data contain multiple wave modes, including body waves and surface waves. Signatures of the tunnel are manifest in the data, refer to the fix locations of receivers, wavefield turbulences can be observed in data recorded by receivers which are close to the top of the tunnel. Consistent noise is evident in the records, for example, in record #1, #6, and #7. The consistent noise might be caused by velocity anomalies corresponding to local infrastructure besides the tunnel. The raw data need to be processed to ensure the stability of the numerical simulation and to increase the imaging quality.

Data pre-processing and Back-scattered signal enhancement.

Routine processing steps, including trace editing and frequency filtering, are applied to the raw data to remove bad traces and to improve the signal-noise-ratio (SNR). Dead and noisy traces are removed from the data set to reduce the influence source clipping and random noise. High-frequency noises are noticeable in the example of record number five (Figure 6b). These noises degrade the data quality and could cause instability to the numerical simulation process. A band-pass frequency filter with passing corner-frequencies 15 Hz and 60 Hz is applied to the entire data set to suppress low-frequency data drifting and high-frequency random noise. After these steps, the P-waves and surface waves are evident in seismograms (Figure 6c). From each trace of the example record of routinely processed data (Figure 6c), the earliest P-wave event appears earlier than the earliest surface wave of which velocity is related to S-wave velocity.

Next, the author utilized slope filter to enhance the backscattered surface waves and attenuate forward propagating waves. The slope filter is a 2D Fourier (frequency-wavenumber; F-k) domain filter that preserves (or eliminates) signals that travel linearly within a certain apparent velocity interval. Consider data $u(x,t)$ and their 2D Fourier domain spectrum $U(k_x,\omega)$

$$u(x,t) \xrightarrow{2D\ Fourier\ transform} U(k_x,\omega).$$

Define wavenumber k_x of an event in F-k domain

$$s_x = \frac{k_x}{\omega} = \frac{1}{v_\omega}. \tag{51}$$

In equation (51), v_ω is the phase velocity at frequency ω of the event to be filtered. Two linear slopes s_{min} and s_{max} are determined from two limiting phase velocities v_{min} and v_{max}, respectively:

$$s_{min} = \left.\frac{dk_x}{d\omega}\right|_{min} = \frac{1}{v_{max}},$$

$$s_{max} = \left.\frac{dk_x}{d\omega}\right|_{max} = \frac{1}{v_{min}}.$$

The slope filter was implemented by applying a fan-shaped taper to the data spectrum:

$$U_{Fk}(k_x,\omega,s_{min},s_{max}) = \begin{cases} \exp(-\epsilon(s_x - s_{max})^2)\,U(k_x,\omega), & if\ s_x > s_{max}, \\ U(k_x,\omega), & if\ s_{max} \geq s_x \geq s_{min}, \\ \exp(-\epsilon(s_{min} - s_x)^2)\,U(k_x,\omega), & if\ s_x < s_{min.} \end{cases} \tag{52}$$

By applying the slope filter, the fan-shaped taper preserves events with a F-k domain slope which is between s_{min} and s_{max}. After slope filtering and transforming back to the time-distance

(x-t) domain, slope filtered data $u_{Fk}(x, t, v_{max}, v_{min})$ and filtering residual $\hat{u}_{Fk}(x, t, v_{max}, v_{min})$ are obtained

$$U_{Fk}(k_x, \omega, s_{min}, s_{max}) \xrightarrow{Inverse\ 2D\ Fourier\ transform} u_{Fk}(x, t, v_{max}, v_{min}). \quad (53)$$

$$\widehat{u_{Fk}}(x, t, v_{max}, v_{min}) = u(x, t) - u_{Fk}(x, t, v_{max}, v_{min}). \quad (54)$$

Figure 7 shows a data processing example in which the slope filter is applied. Figure 7a displays the pre-processed data of record #3. Multiple wave modes can be identified from the pre-processed data: surface waves with low apparent velocities are between x=0 m and x=15 m and between 0.15 s and 0.25 s; an evident back-scattered event can be observed at x=40 m. The 2D Fourier spectrum of these data is displayed in Figure 7c. With two chosen apparent velocities 225 m/s and 1000 m/s, a slope filter is applied to these data and the result are shown in Figures 7b and Figure 7d. The back-scattered events, which provide information about the spatial location of the tunnel, are evident in the filtered data at x=40 m. There is an evident attenuation of the slow surface waves between x=0 m and x=15 m. These results demonstrate that slope filtering can drastically enhance the back-scattered events.

Using equations (53) and (54), data can be decomposed into back-scattered events and forward-going events. An example of data decomposition is displayed in Figure 8 and Figure 9. In these two figures, since the magnitude of 2D Fourier spectrum is symmetric about the origin, the 2D Fourier spectra are folded to show positive k_x- and ω-axis for a close-up view. Using two apparent velocities 225 m/s and 1000 m/s, back-scattered data component and forward-going component are displayed in Figure 8b and Figure 9b, respectively.

In a slope filtering example (Figure 10), the slope filter is used to preserve back-scattered events which have apparent velocities within the 185 m/s to 1200 m/s range. The surface waves with low apparent velocities are similar to the back-scattered surface waves in terms of arrival-time and waveform shape. Therefore, events with apparent velocities less than 185 m/s are excluded from analysis. From the filtered data, the back-scattered surface waves can be identified as the signatures of the tunnel. The back-scattered events suggest that the tunnel is located between 40 m and 50 m from the first station. This observation from the seismic data agrees with the known location of the tunnel.

It can be observed from the slope filtered profile that the back-scattered events are high-SNR signatures of near-surface scatters. Because the slope-filtered data have higher SNR and less interference of wave modes, by using the traveltime and magnitude information contained in the back-scattered events, the spatial location of the near-surface scatters can be accurately retrieved. Therefore, the author proposes a tunnel detection method using the back-scattered surface wave waveform inversion (BSWI). The BSWI can be implemented by straightforward combination of the conventional FWI method with the slope filter. The objective function E of waveform inversion is decomposed with slope-filtered observations and simulations

$$\begin{aligned} \mathrm{E}(\boldsymbol{m}) &= \frac{1}{2}(\delta\boldsymbol{u}_{Fk} + \delta\widehat{\boldsymbol{u}_{Fk}})^T(\delta\boldsymbol{u}_{Fk} + \delta\widehat{\boldsymbol{u}_{Fk}}) \\ &= \mathrm{E}_{\mathrm{Fk}}(\boldsymbol{m}) + \mathrm{E}_{\widehat{Fk}}(\boldsymbol{m}) + \text{cross terms}. \end{aligned} \tag{55}$$

Ignore the cross terms and add a weighting scaler $\beta \in [0,1]$, $\mathrm{E}(\boldsymbol{m})$ can be customized

$$\mathrm{E}(\boldsymbol{m}) \sim \beta\mathrm{E}_{\mathrm{Fk}}(\boldsymbol{m}) + (1-\beta)\mathrm{E}_{\widehat{Fk}}(\boldsymbol{m}). \tag{56}$$

$\mathrm{E}(\boldsymbol{m})$ is sensitive to the back-scattered energy when the weighting factor β approaches 1. However, by Cauchy-Schwartz inequality there is

$$\mathrm{E}(\boldsymbol{m}) \leq \mathrm{E}_{\mathrm{Fk}}(\boldsymbol{m}) + \mathrm{E}_{\widehat{Fk}}(\boldsymbol{m}). \tag{57}$$

Inequality (57) indicates that optimizing $\mathrm{E}_{\mathrm{Fk}}(\boldsymbol{m})$ could lead to increasing of global misfit $\mathrm{E}(\boldsymbol{m})$.

Since objective function $\mathrm{E}_{\mathrm{Fk}}(\boldsymbol{m})$ is sensitive to the back-scattered energy, minimizing $\mathrm{E}_{\mathrm{Fk}}(\boldsymbol{m})$ is helpful to detect scatters which generate back-scattered events. With an emphasis of minimize $\mathrm{E}_{\mathrm{Fk}}(\boldsymbol{m})$ while optimizing global misfit $\mathrm{E}(\boldsymbol{m})$, the BSWI uses both $\frac{\partial \mathrm{E}}{\partial \mathbf{m}}$ and $\frac{\partial \mathrm{E}_{\mathrm{FK}}}{\partial \mathbf{m}}$ – the gradient calculated using the slope-filtered wavefield – in inversion process. The gradient $\frac{\partial \mathrm{E}_{\mathrm{FK}}}{\partial \mathbf{m}}$ which can be viewed as a pre-conditioned $\frac{\partial \mathrm{E}}{\partial \mathbf{m}}$ is used to guide inversion to efficiently image producers of back-scattered energy. Equations (45) is altered to calculate $\frac{\partial \mathrm{E}_{\mathrm{FK}}}{\partial \mathbf{m}}$

$$\begin{cases} \delta\lambda_{Fk} = -\sum\limits_{sources}\int dt\left[\dfrac{(\sigma_{xx}+\sigma_{zz})\left(\Sigma_{xx}^{\mathrm{Fk}}+\Sigma_{zz}^{\mathrm{Fk}}\right)}{4(\lambda+\mu)^2}\right], \\ \delta\mu_{Fk} = -\sum\limits_{sources}\int dt\left[\dfrac{\sigma_{xz}\Sigma_{xz}^{\mathrm{Fk}}}{\mu^2}+\dfrac{1}{4}\left(\dfrac{(\sigma_{xx}+\sigma_{zz})\left(\Sigma_{xx}^{\mathrm{Fk}}+\Sigma_{zz}^{\mathrm{Fk}}\right)}{(\lambda+\mu)^2}+\dfrac{(\sigma_{xx}-\sigma_{zz})\left(\Sigma_{xx}^{\mathrm{Fk}}-\Sigma_{zz}^{\mathrm{Fk}}\right)}{\mu^2}\right)\right]. \\ \delta\rho_{Fk} = -\sum\limits_{sources}\int dt\left(\dfrac{\partial u}{\partial t}\Psi_x^{Fk}+\dfrac{\partial v}{\partial t}\Psi_y^{Fk}\right). \end{cases} \tag{59}$$

In equation (59), $\Sigma_{ij}^{\mathrm{Fk}}$ is the stress of the slope-filtered backward-propagated wavefield. The gradients in terms of geological parameters Vp, Vs, and ρ (47) becomes

$$\begin{cases} \delta Vp_{Fk} = 2\rho Vp\delta\lambda_{Fk}, \\ \delta Vs_{Fk} = -4\rho Vs\delta\lambda_{Fk} + 2\rho Vs\delta\mu_{Fk}, \\ \delta\rho_{\mathrm{Fk}} = (Vp^2 - 2Vs^2)\delta\lambda_{Fk} + Vs^2\delta\mu_{Fk} + \delta\rho_{Fk}. \end{cases} \tag{60}$$

And the model updating process (48) becomes

$$\begin{cases} \mathrm{V_p^{n+1}} = \mathrm{V_p^n} + \theta_p^n \delta V p_{Fk}^n, \\ \mathrm{V_s^{n+1}} = \mathrm{V_s^n} + \theta_s^n \delta V s_{Fk}^n, \\ \rho^{n+1} = \rho^n + \theta_\rho^n \delta \rho_{Fk}^n. \end{cases} \quad (61)$$

For each iteration, the BSWI tries to update model with $\frac{\partial \mathrm{E_{FK}}}{\partial \mathbf{m}}$, if no optimizing step length is found then this iteration will start over and model will be updated with $\frac{\partial \mathrm{E}}{\partial \mathbf{m}}$. Using this strategy, the BSWI intends to speed up the inversion process by using a pre-conditioned gradient $\frac{\partial \mathrm{E_{FK}}}{\partial \mathbf{m}}$. In the worst cases which $\frac{\partial \mathrm{E_{FK}}}{\partial \mathbf{m}}$ leads to local minima, the BSWI updates model in such a manner as to guarantee that the overall error $\mathrm{E}(\boldsymbol{m})$ does not magnify. The workflow of BSWI method is illustrated by Figure 11. This thesis proposes to demonstrate that the BSWI can detect velocity anomalies efficiently by focusing on minimizing the misfit in the back-scattered waveforms. In the next chapter, the author demonstrates with examples that the BSWI method can speedup anomaly-detecting process.

Chapter IV: Results

In this chapter, the BSWI method is applied to numerical and real-world data sets to study the feasibility of this method.

Numerical experiments

The BSWI method is tested with a numerical example. The proposed BSWI is compared with the conventional FWI method at a setting that includes a subsurface void and complicated scattering and dispersion caused by irregular topology. The true model and the initial model are displayed in Figure 12. In the true Vs model, there is a low-Vs (250 m/s) anomaly located at x=50 m with its center located 7.5 m deep. There is an irregular subsurface interface at the top of the true model. The irregular topography of the interface (Almuhaidib and Toksöz, 2014) was created using a set of random numbers generated by a Gaussian distribution with 5 m mean and a standard deviation of 5 m. Complicated scattering and dispersion will be produced by this irregular interface during the wavefield simulation. For the initial model, the depth of the top subsurface interface was set to 5 m which equals the mean depth of the irregular interface.

The synthetic data have eight shot-gathers with a source spacing of 10 m. The first shot is located at x=10 m. Forty-eight receivers are fixed on the free surface from x=10 m to x=70.5 m with a 1.5 m interval. A 45 Hz Gaussian derivative wavelet is used as the source signal. To simulate field conditions, series of Gaussian white noise was added to the synthetic data. Figure 13a displays an example of synthetic shot-gathers. From it, we can observe the dispersion in the surface waves resulting from the irregular interface. We can also observe the back-scattered events coming from the Vs-anomaly and the irregular interface.

The conventional FWI and the proposed BSWI were implemented on these synthetic data in order to detect the low-Vs anomaly. For both methods, the synthetic data were directly used without processing. These two methods are controlled by the preconditioned conjugate gradient (PCG) method with the same set of inversion parameters except for the use of the slope filter in the BSWI. We allow each inversion method to run through five iterations to determine which method is superior in efficiency. Figures 13b and 13c are showing the simulated waveforms at the end of the fifth iteration of the FWI and the BSWI, respectively. Compared with the waveforms simulated by using the conventional FWI method, the result from the BSWI method has less misfit in the back-scattered surface waves which are highlighted with black dashed boxes in Figure 13. However, the simulated waveforms from the conventional FWI method have less misfit in the forward-going surface waves which are highlighted with red dashed boxes in Figure 13.

The difference in optimization between the two methods can also be noticed in the inverted Vs profiles (Figure 14) and calculated gradients (Figure 15) correspond to the first five iterations. Since having greater amplitudes than the back-scattered events, the forward-going surface waves have larger weights in the objective function. Therefore, the conventional FWI method minimizes the objective function by refining the Vs model where the irregular interface was present. On the contrary, because of its objective function is designed to be sensitive to the back-scattered waves, the BSWI method is focused on imaging the velocity anomalies which generate the back-scattered events.

For this numerical example which is simple in its velocity structure and has a single anomaly, both inversion methods converged and produce accurate inverted velocity profiles after 50 iterations (Figure 14, last row). However, the BSWI method has demonstrated its ability to

efficiently detect near-surface scatters when the data have complicated scattering and surface-wave dispersion.

Field experiments

The subsurface velocity structure of site where the field data was collected is unknown. Therefore, the initial velocity model needs to be estimated before utilization of waveform inversion methods. The Rayleigh wave first-arrival refraction tomography method is used first for creating the initial Vs model. Then, the conventional FWI and the proposed BSWI method are applied to the field data.

Initial model building

Firstly, initial Vs velocity is estimated using a ray-theory-based refraction tomography method (Koulakov, Stupina, & Kopp, 2010). The sensors used for this research are vertical geophones which measures the vertical motion or acceleration of the ground. Therefore, the sensors can hardly record the pure shear waves of which the particle motion is horizontal along the surface. However, for linear elastic materials with positive Poisson ratio ($\gamma > 0$), the surface wave (Rayleigh wave) phase speed are tightly related with the shear wave speed (Freund, 1998). This property enables us to perform joint analysis of refractions with surface waves to obtain shear wave velocity (Ivanov et al., 2013). This tomography method iteratively minimizes the difference in first-arrival travel-times between the observation and simulation. The travel-times between the two surface points of the velocity model along possible ray paths are calculated by bending rays between these two points. By choosing the minimum from all calculated travel-times, the first-arrival travel-time is obtained for the two surface points.

The observed Rayleigh wave travel-times are manually picked (Figure 16) from the acquired seismic data. The tomography converges within thirty iterations (Figure 17). An area of low velocity (300 m/s) is evident on top of the tomography result (Figure 17f) between 50 m and 55 m. At late iterations starting from iteration #25, high-velocity (>850 m/s) anomalies can be observed between x= 50 m and x=60 m from the tomography results. These high-velocity anomalies are indicating the concrete walls and base of the tunnel. In the comparison between observed Rayleigh wave travel-times and simulated travel-times at the 30^{th} iteration (Figure 18), the overall fitting is good which demonstrates that the background Rayleigh wave velocity is successfully retrieved by the travel-time tomography. The error in travel time decreases rapidly with increasing of the iteration number (Figure 19).

The obtained Rayleigh wave velocity profile is directly used as the initial Vs model. A lateral-homogeneous model (Figure 20a) is created by smoothing the background of the result of Rayleigh wave travel-time tomography. By starting inversion from a lateral-homogeneous model and ignoring velocity anomalies in the Rayleigh wave travel-time tomography results, the influence of the tomography to the waveform inversions is avoided.

Conventional FWI results

Next, with the initial Vs model estimated by travel-time tomography, conventional FWI is applied to the pre-processed data. We set the location of the first station at x=10 m to allow additional model space for the perfectly matched layer (PML) absorbing boundary condition. According to the known site conditions, we expect to detect the tunnel between x=50 m and x=55 m.

After 100 iterations, the inverted Vs is obtained by the conventional FWI (Figure 20). Detected tunnel location (Figure 21) is estimated by highlighting low-Vs (Vs<300 m/s) areas of the Vs profile obtained at the 100^{th} iteration (Figure 20f). It shows a low-Vs anomaly with its center located at x=51 m, z=-5 m after 100 iterations. Considering the true depth of the tunnel is approximately 2.5 m, the detected location is deeper, and its shape is elongated and dipping. Imaging artifacts can be observed from the FWI result. The low imaging resolution and convergence rate might be caused by the complexed structures which consist of void, concrete walls, and concrete sidewalks.

A waveform comparison (Figure 22) was used to improve the reliability of the inversion results through comparisons of pre-processed and simulated data. Both pre-processed and simulated data are normalized trace-by-trace. From comparisons at iteration #1 (Figure 22a) and iteration #100 (Figure 22b), there is an evident improvement in waveform fitting between trace #20 and #35, which are the traces over the top of the tunnel.

Improve FWI result with data tapering

To improve the result from the conventional FWI, we apply an additional data processing step – tapering. The travel-time of the early surface waves are manually picked for each shot-gather. Time window functions (Tapers) based on the picked travel-times are applied to preserve only the early surface waves. The tapering example of two data records - record #1 and #3 - are displayed in Figure 23. A comparison between pre-processed data and tapered data is shown by Figure 24. It can be observed from the data comparison that the tapered data contain less noise. The detected location of the tunnel is displayed in Figure 25. The FWI of the tapered data has reduced the imaging artifacts and improved the resolution of the tunnel's image at the cost of

additional processing. In practice, data processing could be time-consuming and demanding. A waveform comparison between tapered data and simulated data is displayed in Figure 26.

BSWI results

Finally, the BSWI method was tested using the data without additional processing. The inverted Vs profiles corresponding to the first five iterations are displayed in Figure 27. After 30 iterations, the BSWI inverted Vs profile (Figure 31d) shows a clear image of the tunnel with its center located at x=52 m, z= -2 m. The imaging artifacts can be observed at x= 70 m and between x=30 m and x= 40 m. They could be caused by the shallow infrastructure below the concrete sidewalk. However, these artifacts have lower magnitudes than the tunnel.

Figure 29 and Figure 30 display comparisons of the waveforms of pre-processed data and simulated data at the 30th iteration of BSWI for record #3 and #7, respectively. The source locations of the shot-gathers for displaying are located on both sides of the tunnel. In Figure 29 and Figure 30, panels a) and c) display the pre-processed data used for BSWI, unfiltered and slope filtered, respectively. And panels b) and d) display the simulated waveforms at the 30^{th} iteration, unfiltered and slope filtered, respectively. These results of waveform comparison indicate that, in the regular data domain, the misfit in the waveforms has complicated modes due to the interference caused by the surface waves and the scattering events from off-line objectives. However, in the slope-filtered data domain, the tunnel's signatures are clear and the misfit between the observations and simulations has simple modes. These inversion results demonstrate that the BSWI is capable of efficiently detecting a near-surface tunnel with the minimum amount of data processing which lends it as a method suitable for application in the field. The inverted Vs profiles by using different method are illustrated in Figure 31. Refer to the true location of the tunnel (Figure 31a), three waveform inversion methods applied have successfully detected the

target. However, the difference in resolution of obtained Vs profiles is evident: the inverted Vs from conventional FWI method (Figure 31b) has a deeper detected location of the tunnel and an artificial high-Vs zone; while inverted results from FWI using the tapered data and BSWI using the pre-processed data display accurate detected locations of the tunnel and contain less imaging artifacts.

Chapter V: Discussion

Through a series of studies of waveform inversion theorem and back-scattered surface waves, the author reviewed the fact that near-surface scatters can be efficiently detected by using the back-scattered surface waves which are evident in frequency-wavenumber domain and can be retrieved with slope filtering. Therefore, this thesis proposed and studied a new method to efficiently detect near-surface velocity anomalies. The proposed method implements waveform inversion of back-scattered surface waves (BSWI).

The numerical example demonstrates that BSWI method is capable of efficiently detecting a near-surface tunnel by focusing on optimizing back-scattered surface wave events. The efficiency of BSWI method comes from taking advantage of information contained in the back-scattered events. The author uses comparisons between BSWI and conventional FWI in terms of inverted velocity profile and calculated misfit gradient to illustrate the difference of optimization preference. However, the efficiency come at the cost of neglecting information contained in forward-going events. Consequently, the BSWI method might not be suitable for refining an accurate subsurface velocity model. Additional work is needed to resolve this limitation. In the future, the author proposes to combine BSWI and conventional FWI in a way that the BSWI is utilized at early iterations to locate velocity anomalies and the FWI is used during late iterations to refine the velocity model.

A successful application of BSWI to the real-world data is illustrated by the field data example. Compared with conventional FWI, which is either low in rate of convergence or demanding extraordinary data quality, BSWI provides an accurate but less demanding solution to near-surface tunnel detection tasks. From the inverted Vs (Figure 31d) by using BSWI, multiple low-Vs anomalies can be identified. Further research is needed to study those detected anomalies

aside the one which denotes the tunnel. They could be caused by shallow infrastructure below the concrete sidewalk or other off-line objectives.

To conclude, the BSWI method has demonstrated its ability to efficiently detect near-surface scatters when the data have complicated scattering and surface-wave dispersion. Especially, BSWI's characteristic of efficient imaging has revealed the potential of developing an effective in-situ tunnel detecting workflow when time-consuming data processing steps are needed by the conventional FWI.

Figures

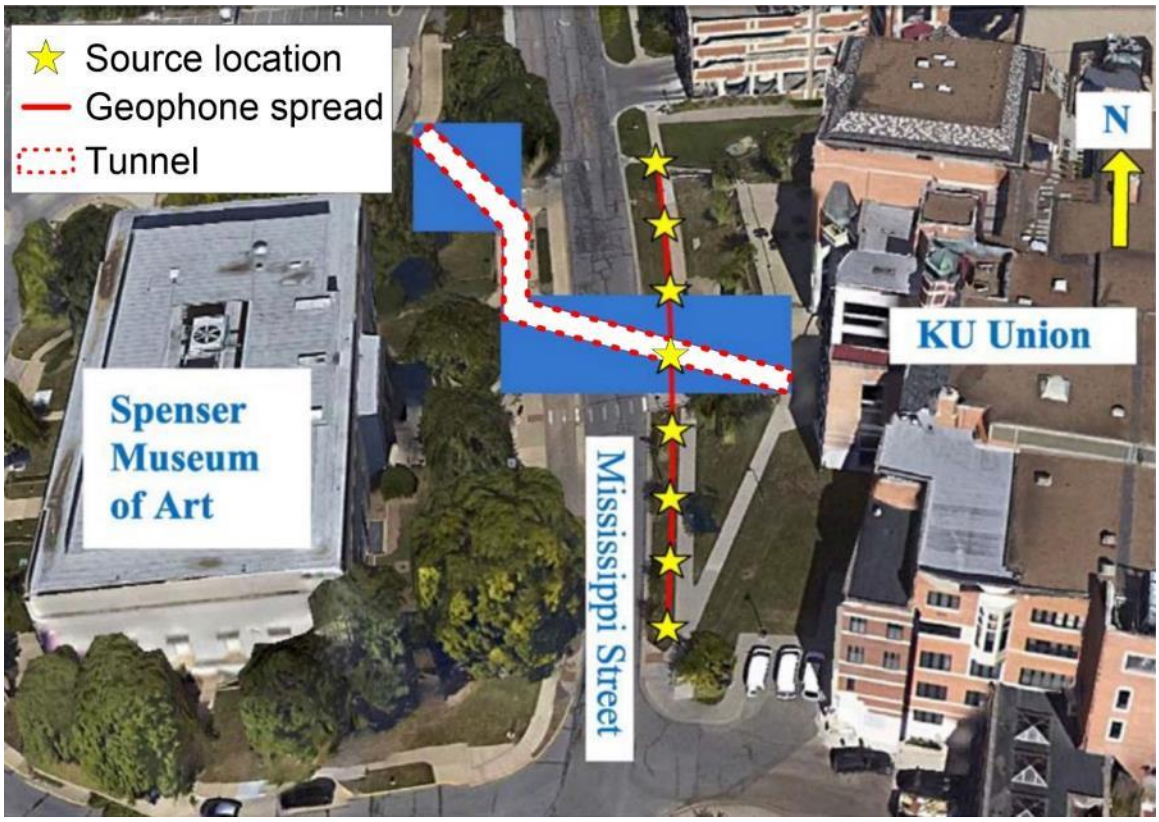

Figure 1. An overview of the site and the 2D seismic survey. Modified from Shao et al. (2016).

Figure 2. A close-up of the 2D seismic survey at the south end of the receiver spread (Left) and over the tunnel where the geophones are equipped with metal bases and placed on the concrete sidewalk (Top).

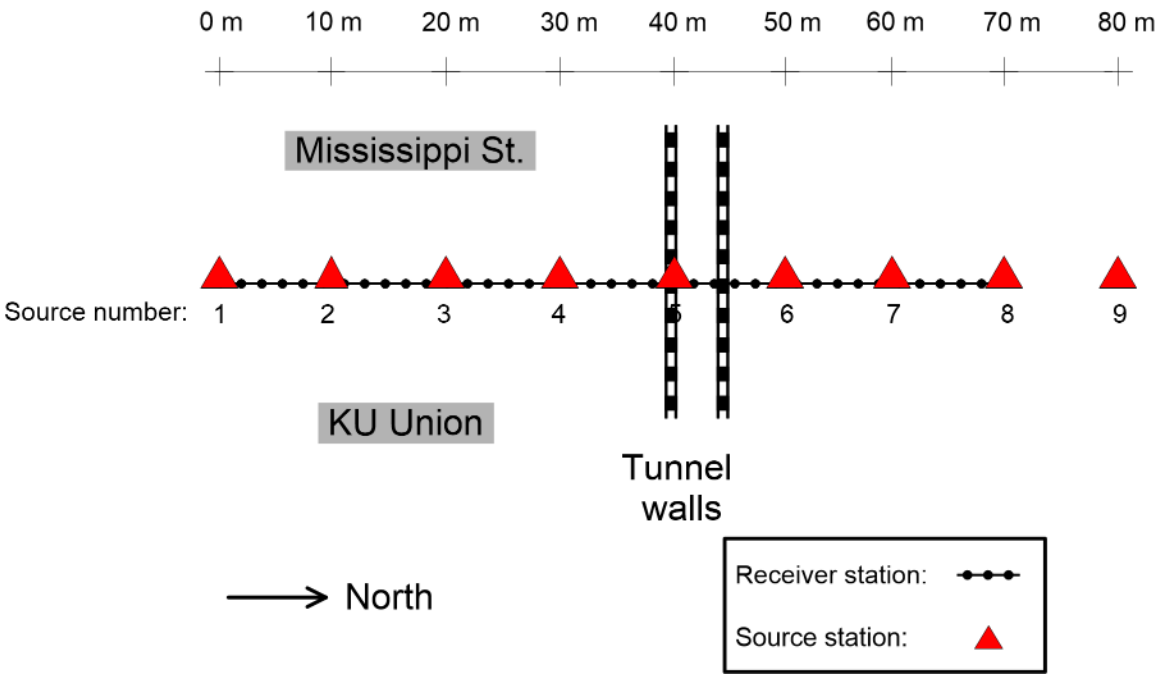

Figure 3. The geometry of the 2D seismic observation system.

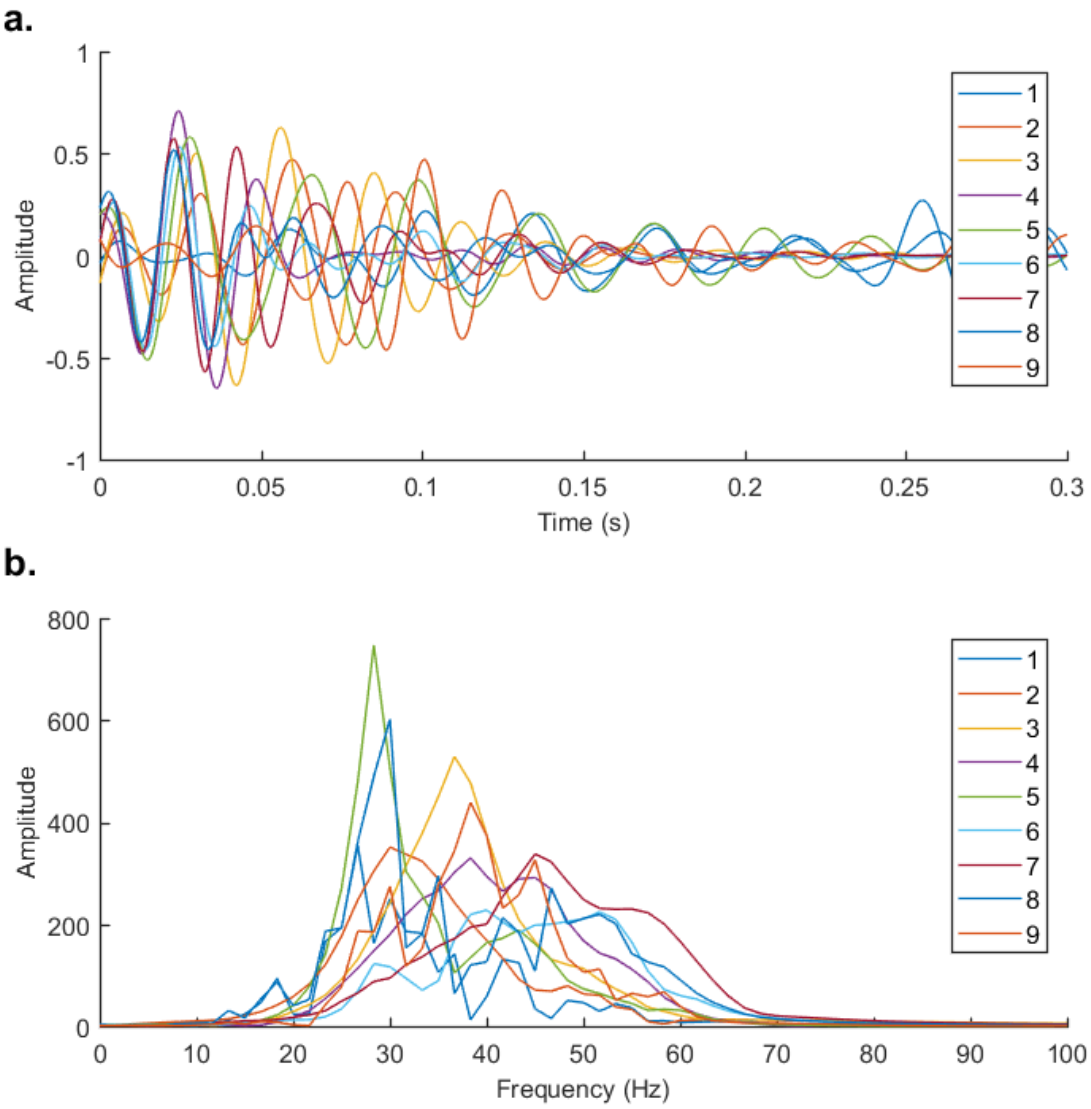

Figure 4. Source signals with record number displayed in legend: (a) Source signal (Pilot trace) for each record in time domain, and (b) source signal spectra in frequency domain.

a.

b.

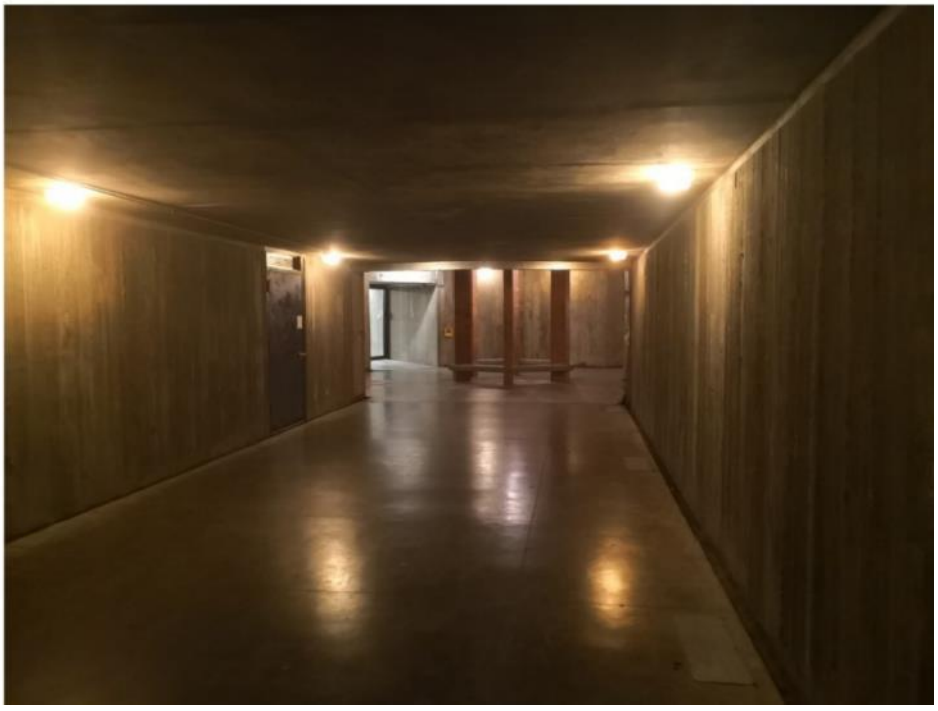

Figure 5. Interior of the tunnel (a) beneath the 2D seismic survey line, and (b) beneath Mississippi St.

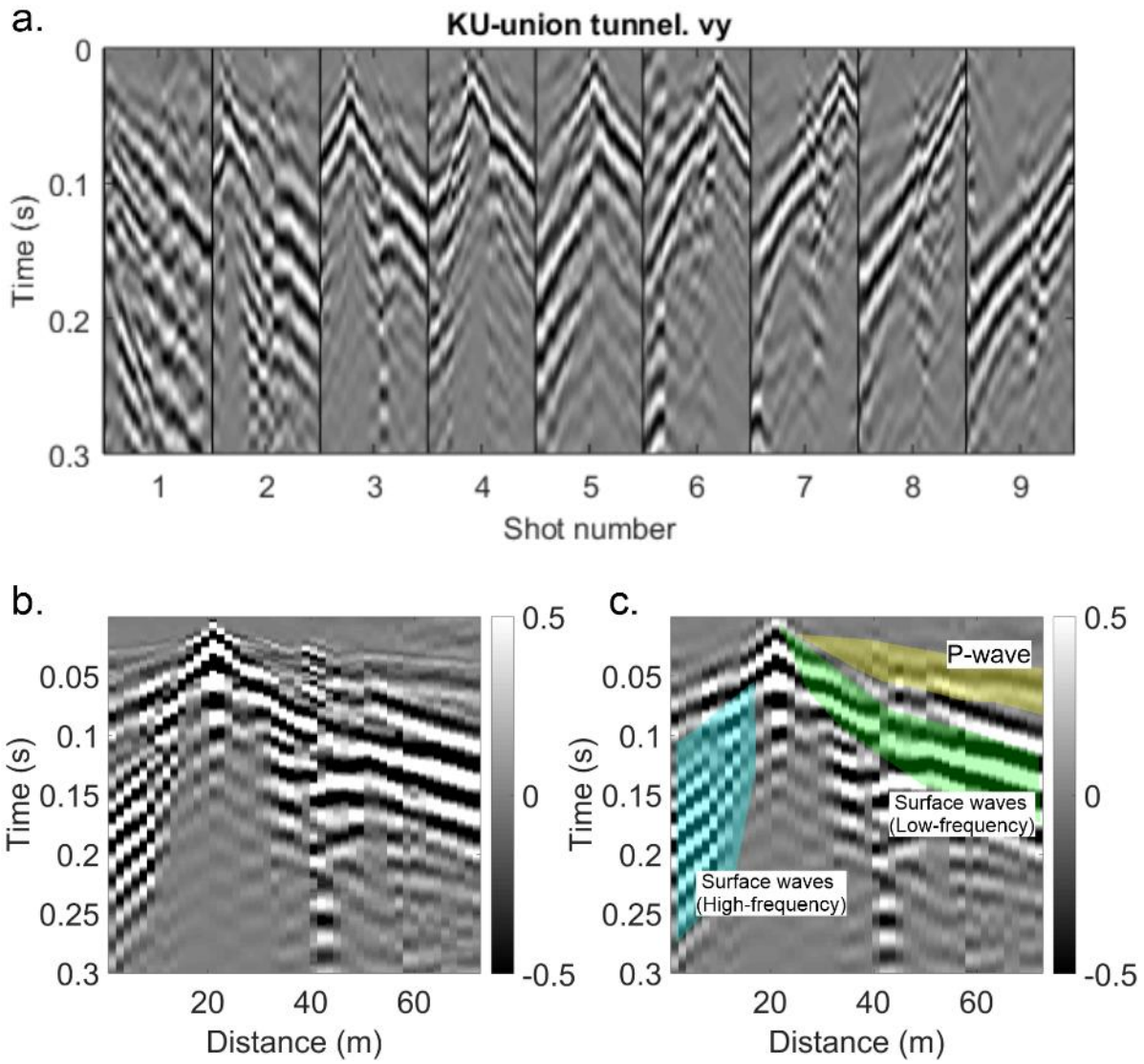

Figure 6. The vertical-component data acquired by the 2D seismic survey and an example of data routine processing. (a) The raw data which contain nine records. The x-axis is shot (record) number. Each record contains forty-eight traces. (b) Raw data of record number five (record #5). (c) Routinely processed data of record number five. Three types of typical event including compressional wave (P-wave), low-frequency surface waves, and high-frequency surface waves are highlighted with yellow, green, and cyan colors, respectively.

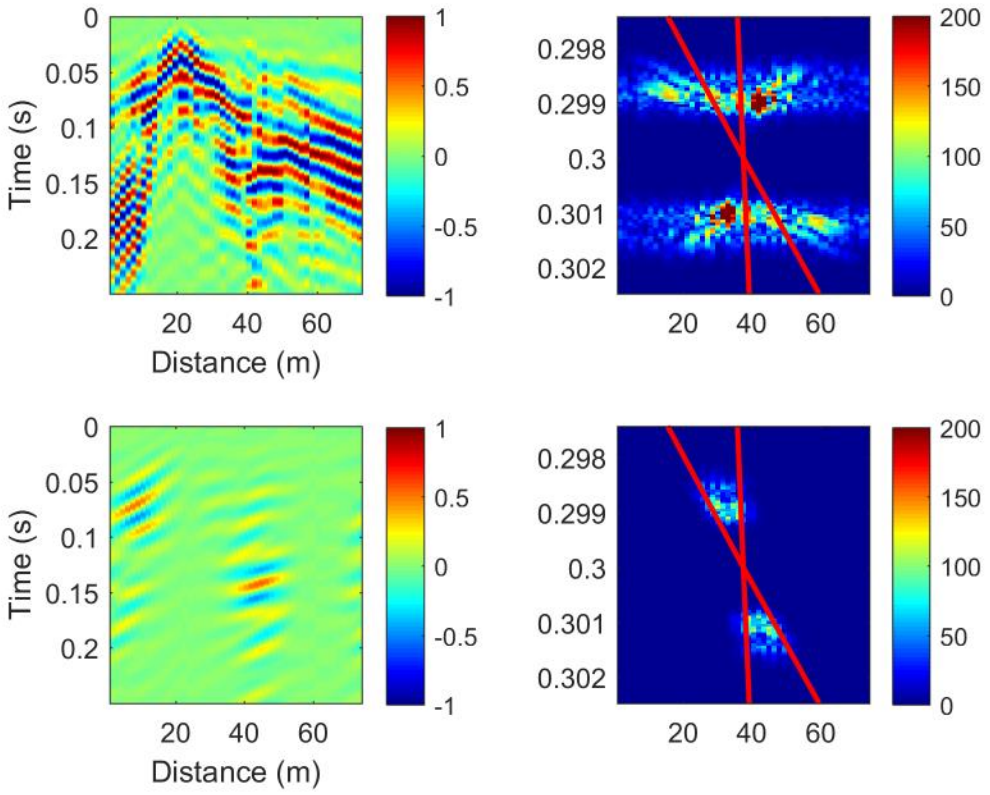

Figure 7. Example of back-scattered events enhancement with slope filter. (a) Pre-processed data of record #3. (b) F-k filtered data of record #3. (c) Full 2D Fourier spectrum of record #3. Two red lines in this panel denote apparent velocity 225 m/s and 1000 m/s, respectively. (d) Full F-k filtered 2D Fourier spectrum of record #3. Two red lines in this panel denote apparent velocity 225 m/s and 1000 m/s, respectively.

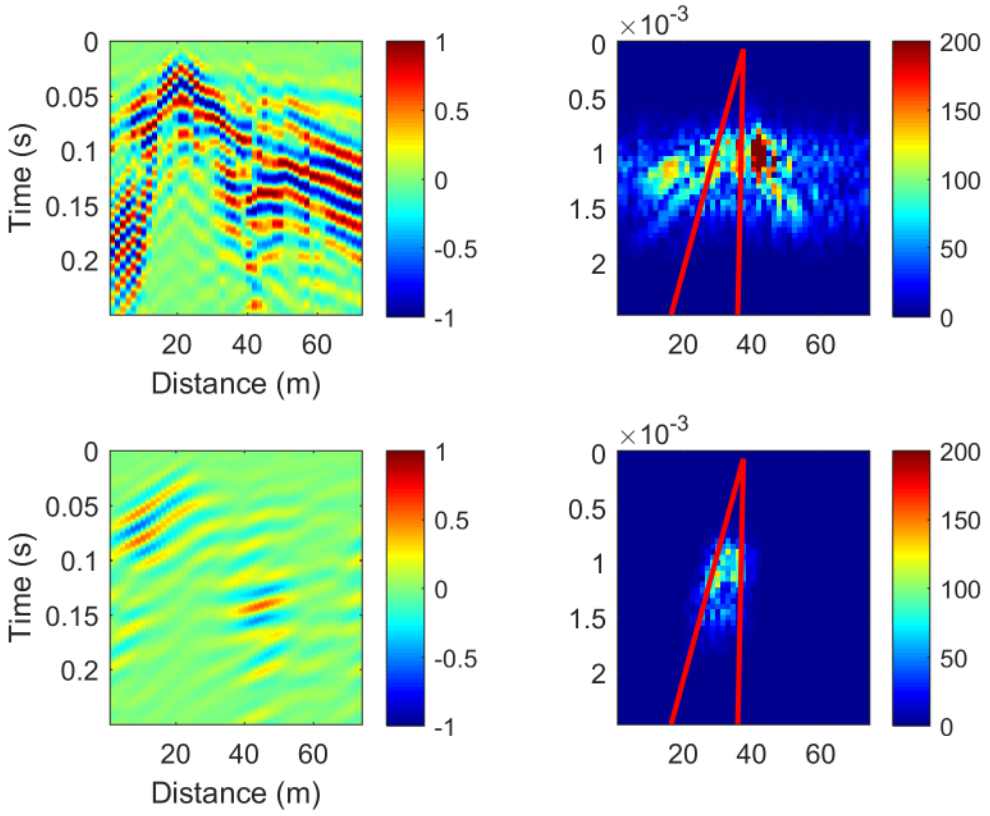

Figure 8. Example of back-scattered events enhancement with slope filter. (a) Pre-processed data of record #3. (b) F-k filtered data of record #3. (c) Folded 2D Fourier spectrum of record #3. Two red lines in this panel denote apparent velocity 225 m/s and 1000 m/s, respectively. (d) Folded F-k filtered 2D Fourier spectrum of record #3. Two red lines in this panel denote apparent velocity 225 m/s and 1000 m/s, respectively.

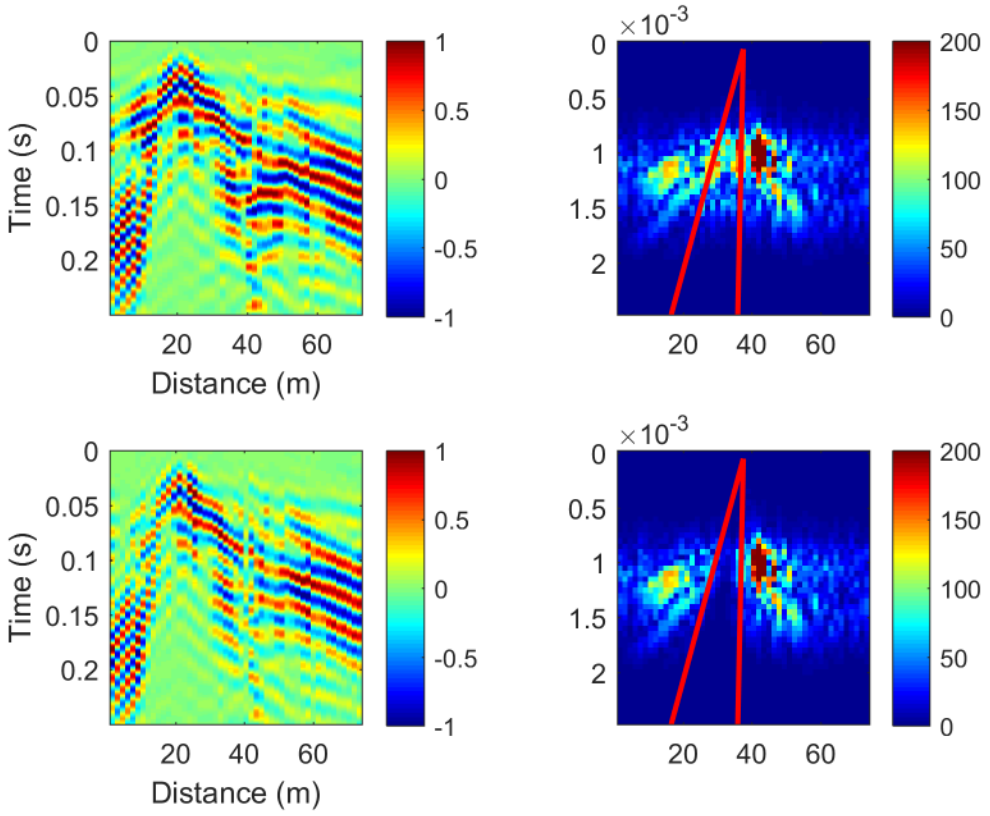

Figure 9. Residual of slope filtering. (a) Pre-processed data of record #3. (b) F-k filtered data of record #3. (c) Folded 2D Fourier spectrum of record #3. Two red lines in this panel denote apparent velocity 225 m/s and 1000 m/s, respectively. (d) Folded F-k filtered 2D Fourier spectrum of record #3. Two red lines in this panel denote apparent velocity 225 m/s and 1000 m/s, respectively.

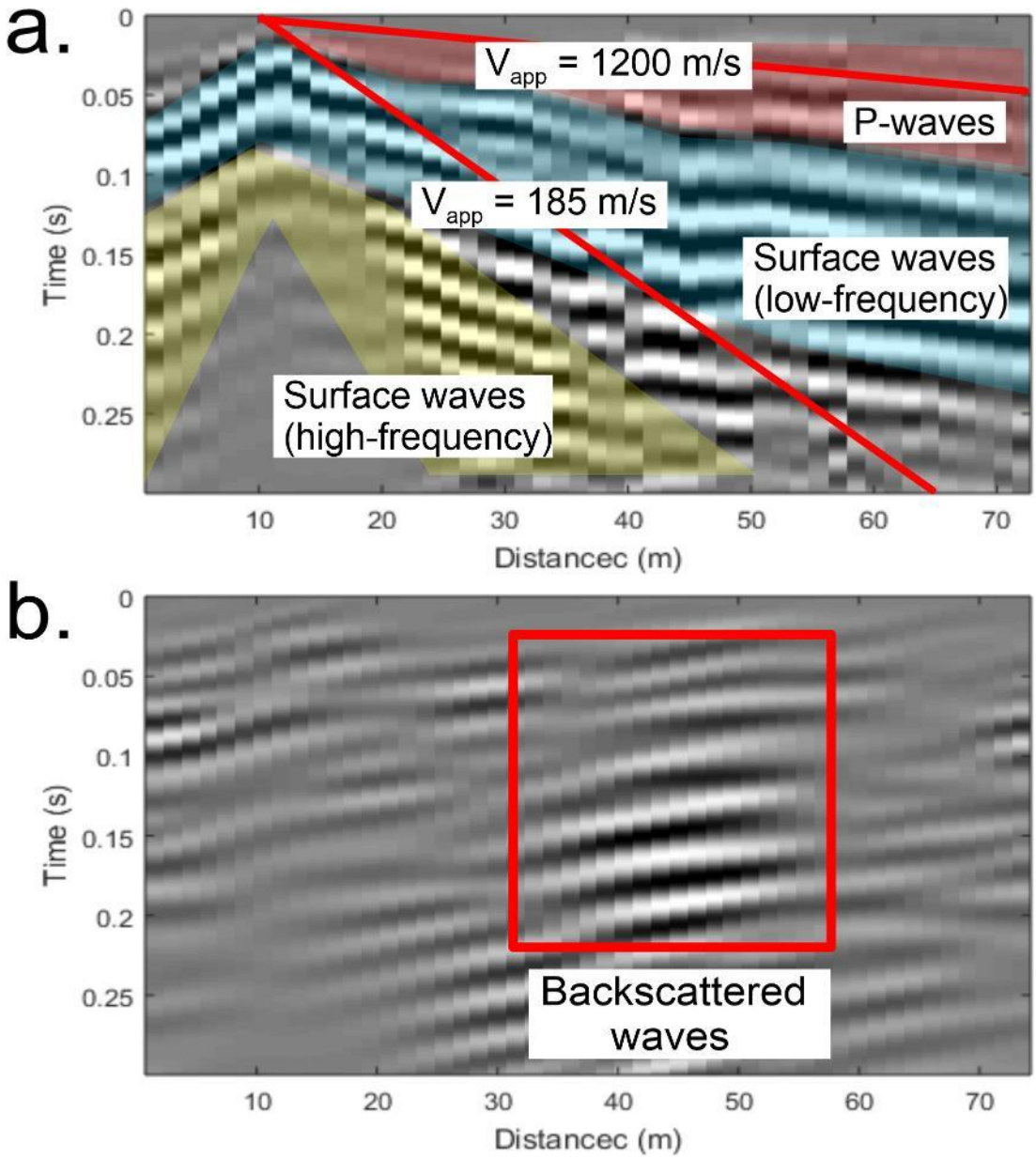

Figure 10. Data processing examples. a) Pre-processed data. Two red lines are indicating the first-arrival times for apparent velocity 1200 m/s and185 m/s, respectively. b) Pre-processed data after slope filtering. The red box is highlighting the backscattered waves which are enhanced after slope filtering.

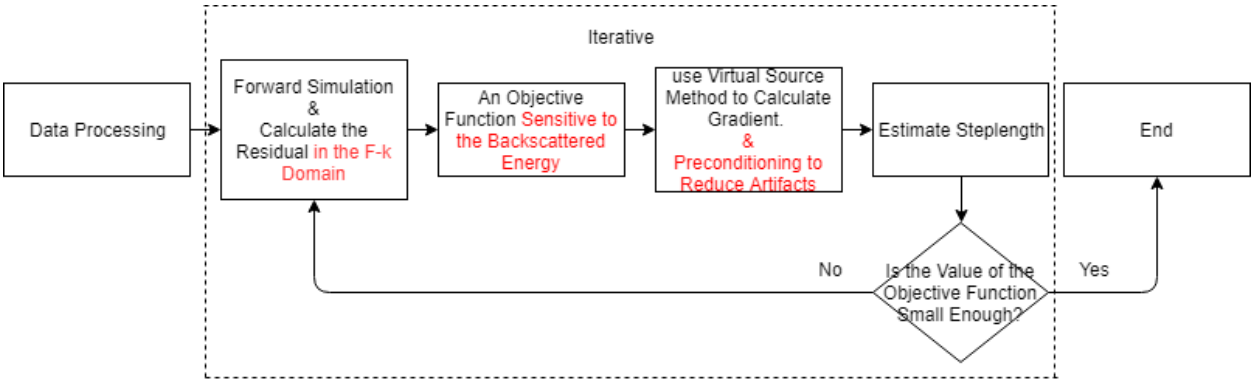

Figure 11. BSWI workflow.

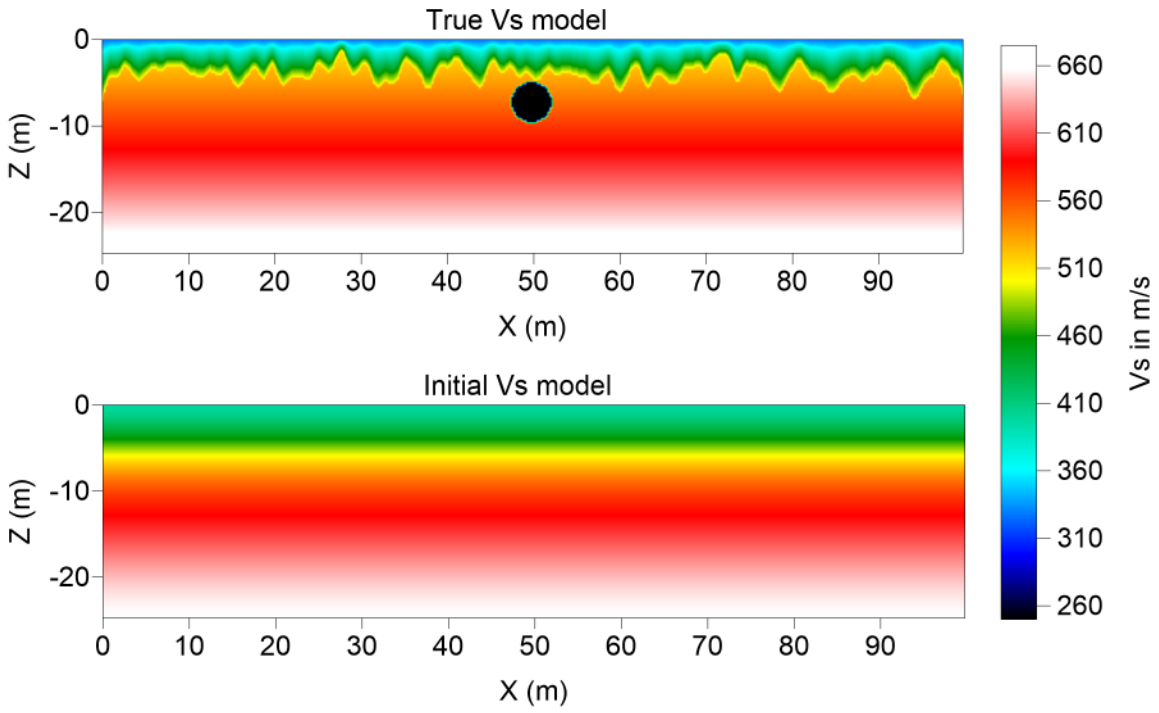

Figure 12. The true (a) and initial (b) Vs model used by the single-void numerical example.

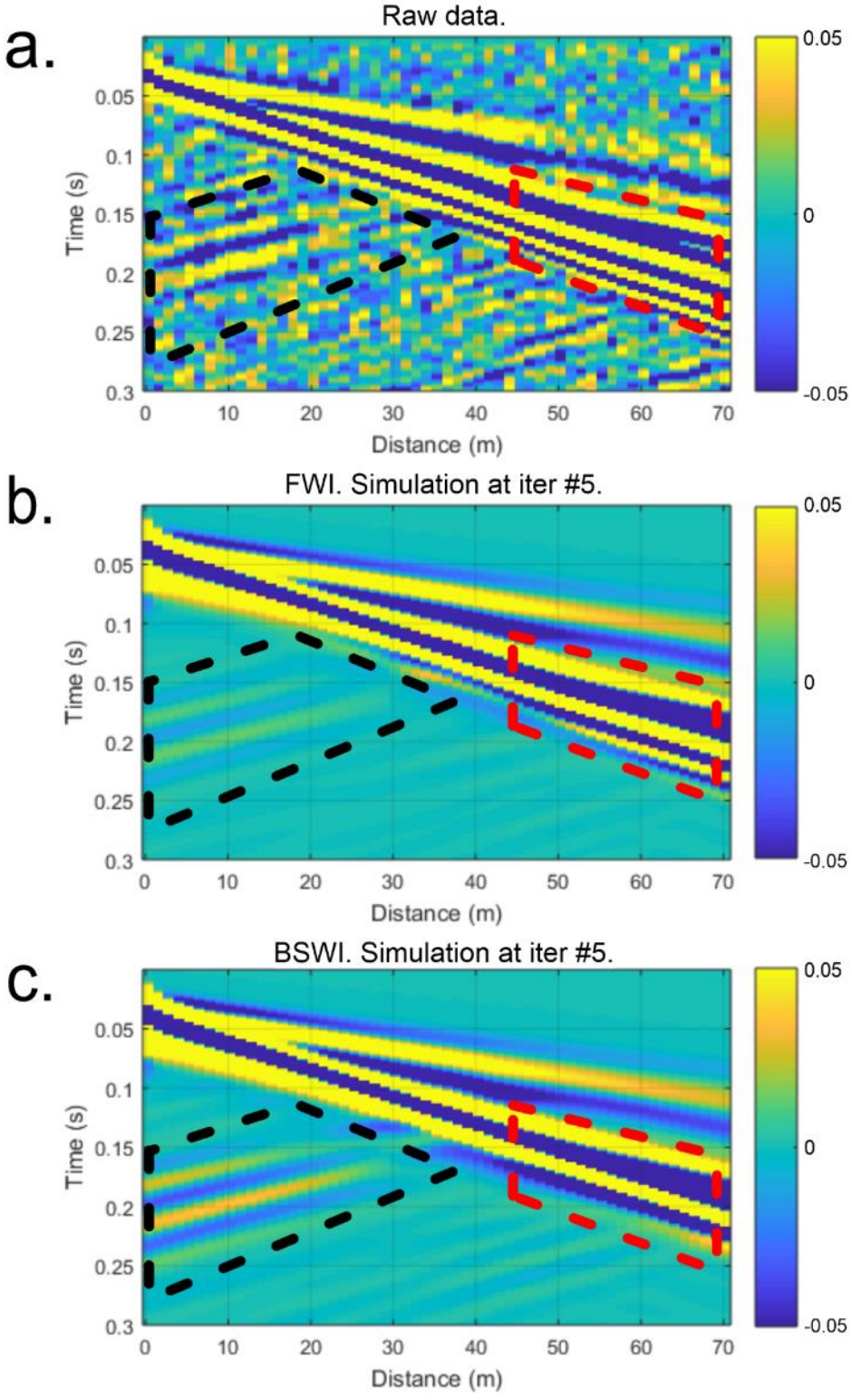

Figure 13. Synthetic data example showing a) simulated field data, b) FWI simulated waveforms and c) BSWI simulated waveforms.

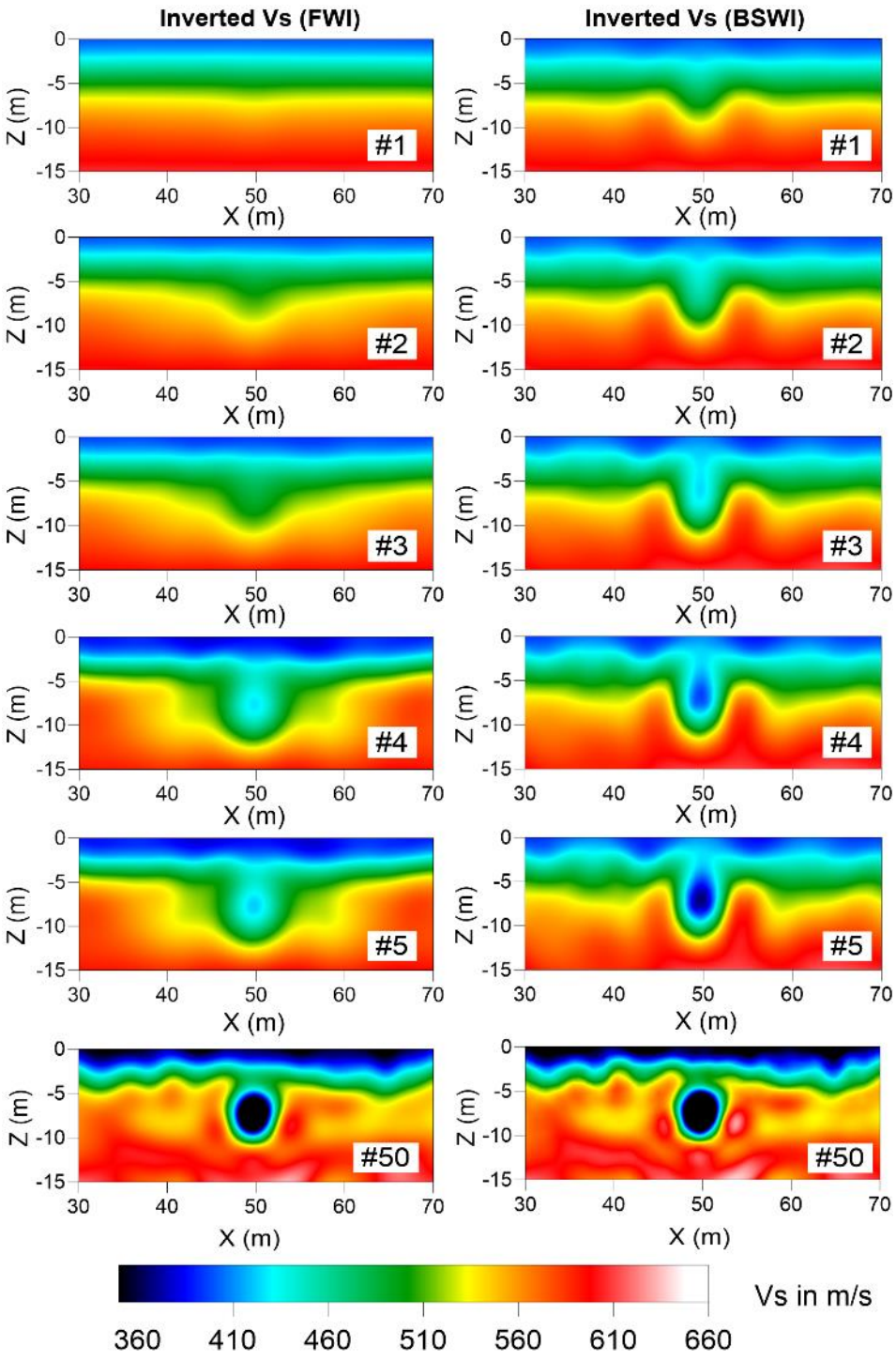

Figure 14. Results of the inverted Vs within the first five iterations by using the conventional FWI (left column) and the BSWI (right column). The iteration number is at the right-bottom corner of each panel.

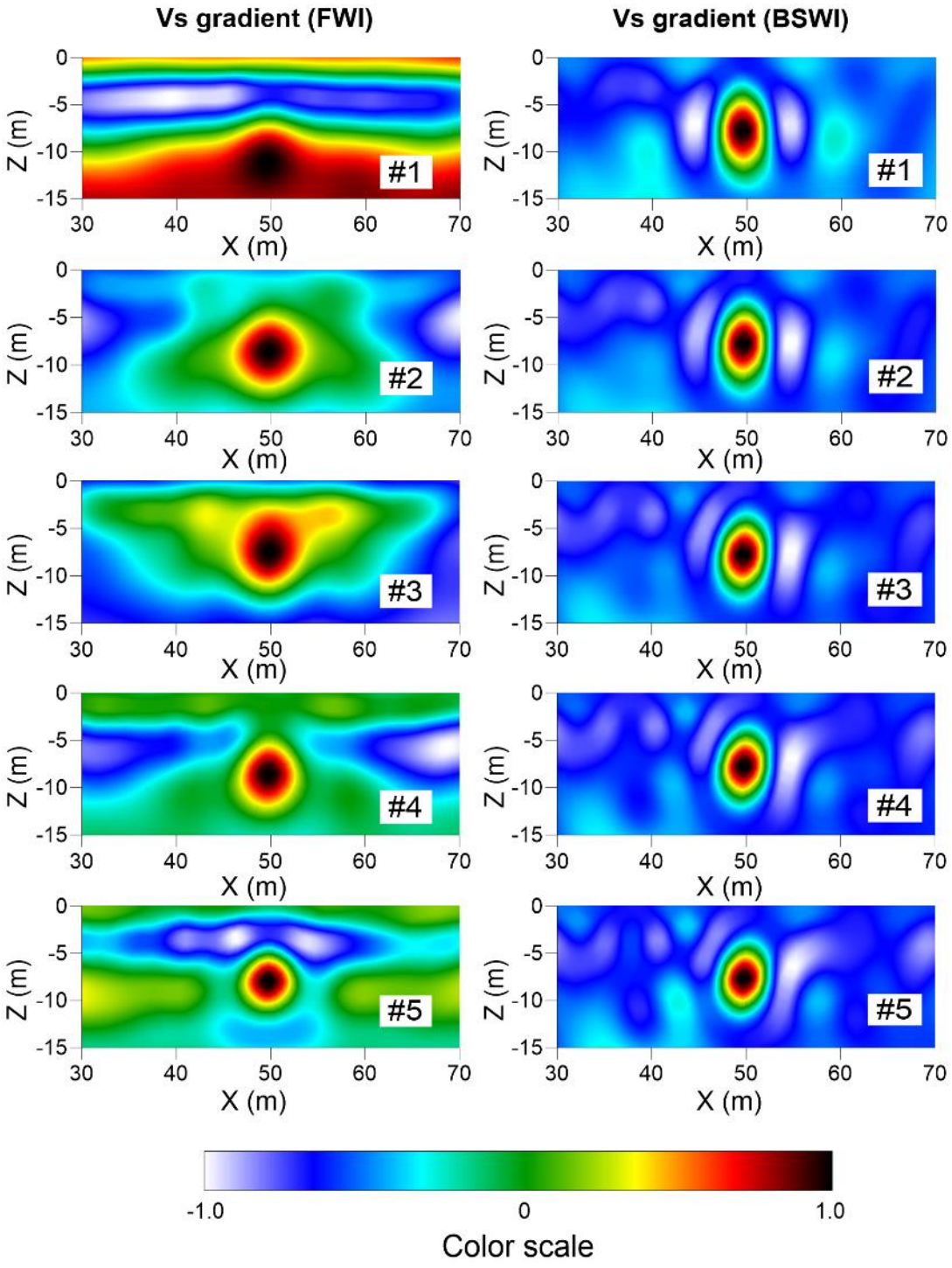

Figure 15. Results of the Vs gradient within the first five iterations by using the conventional FWI (left column) and the BSWI (right column). The iteration number is at the right-bottom corner of each panel.

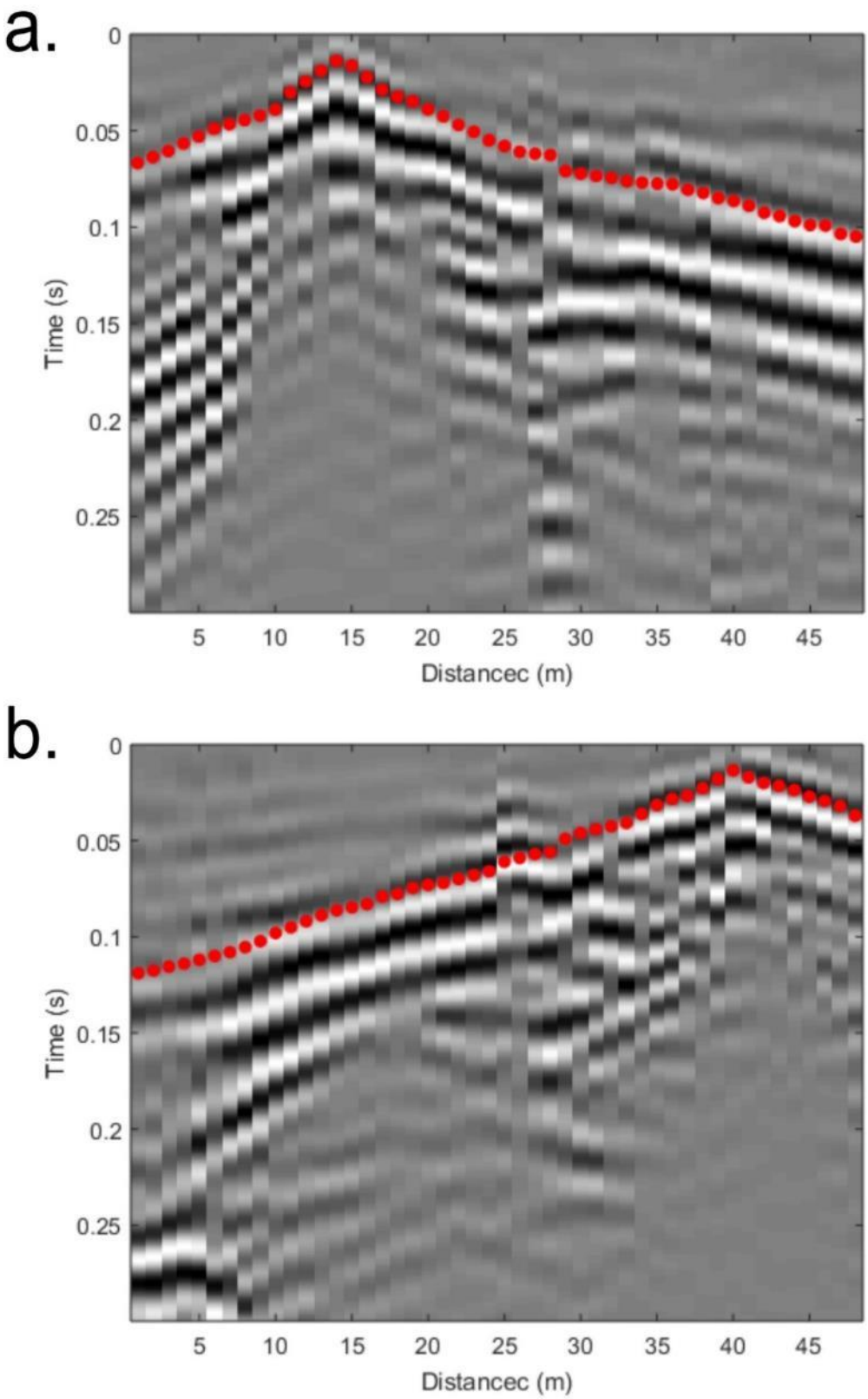

Figure 16. Picked surface wave travel times (red dots) for (a) record #3 and (b) record #7.

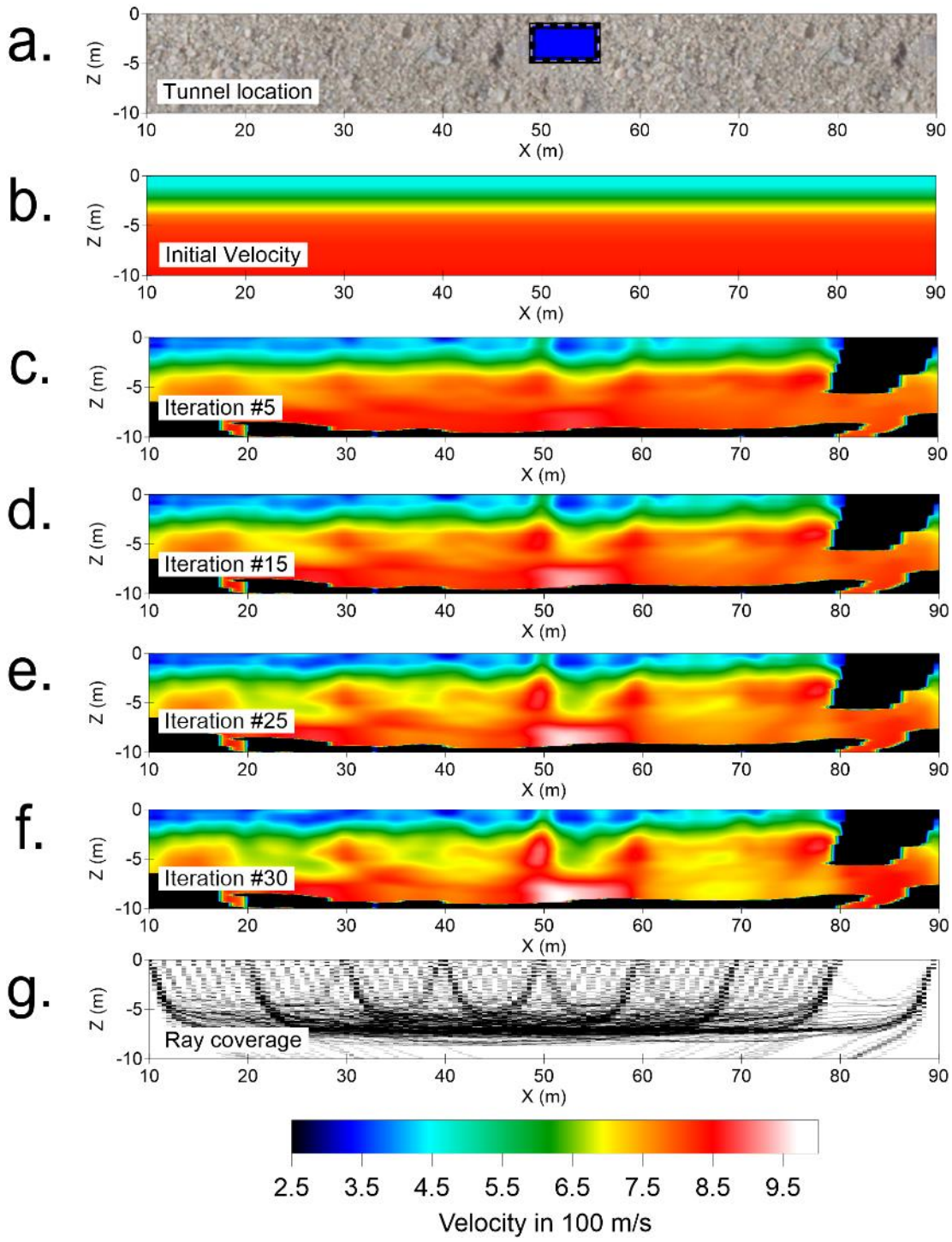

Figure 17. Surface wave travel-time tomography. (a) Location of the tunnel. (b) Initial velocity model. Inverted velocity profiles are displayed after (c) 5, (d) 15, (e) 25, and (f) 30 iterations. (g) The ray coverage of the travel-time tomography.

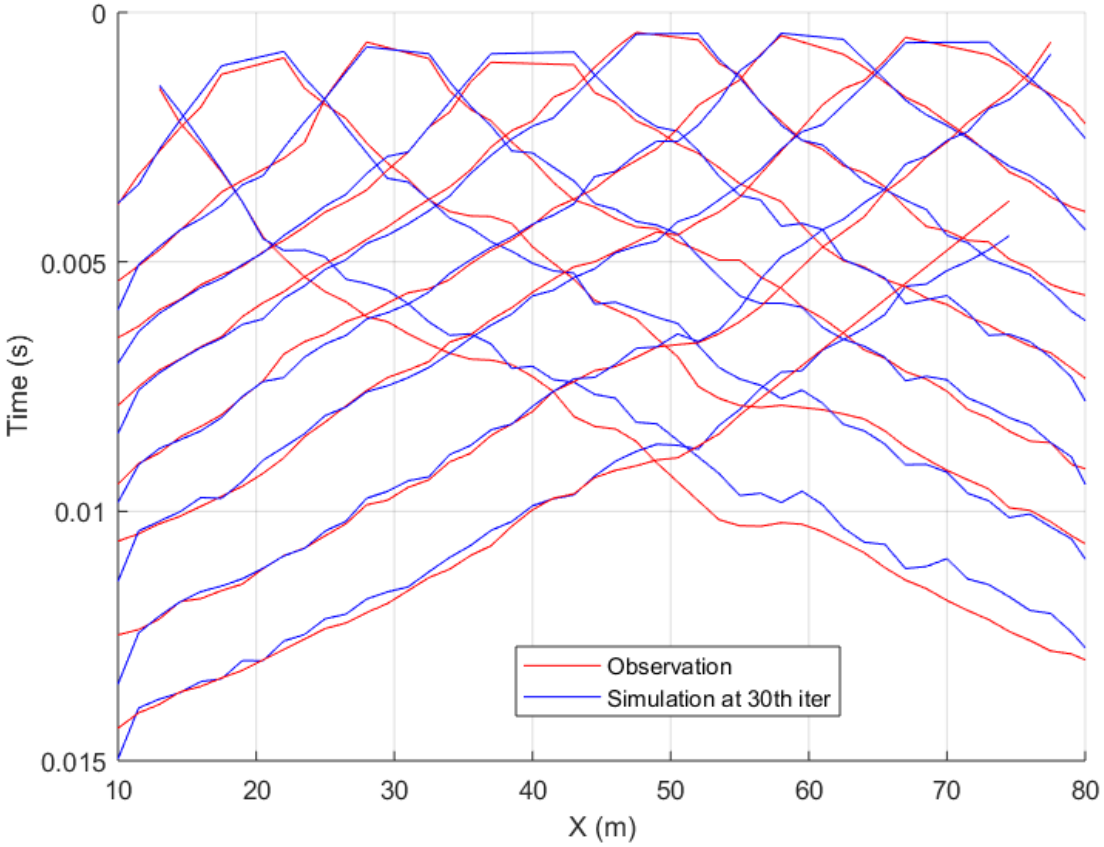

Figure 18. Observed surface wave travel-times (blue) and simulated surface wave travel-times at 30th iteration (red).

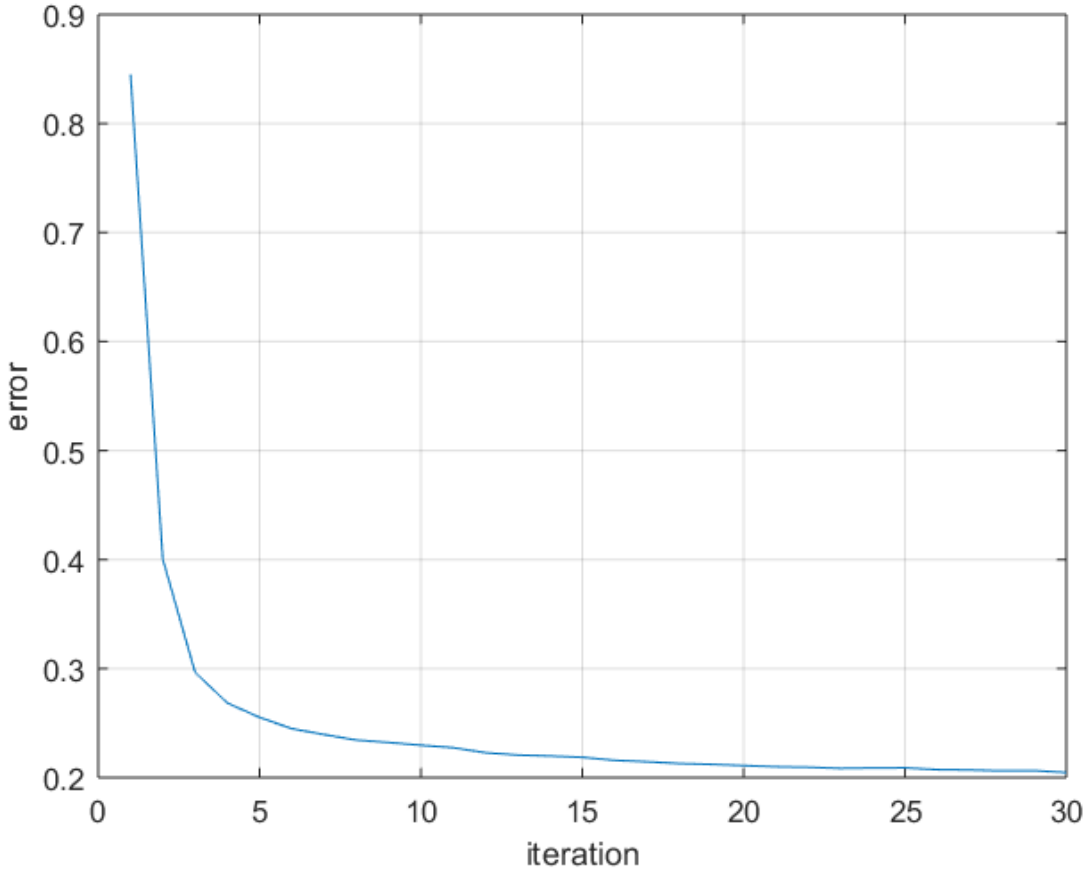

Figure 19. Travel-time tomography error vs. iteration curve.

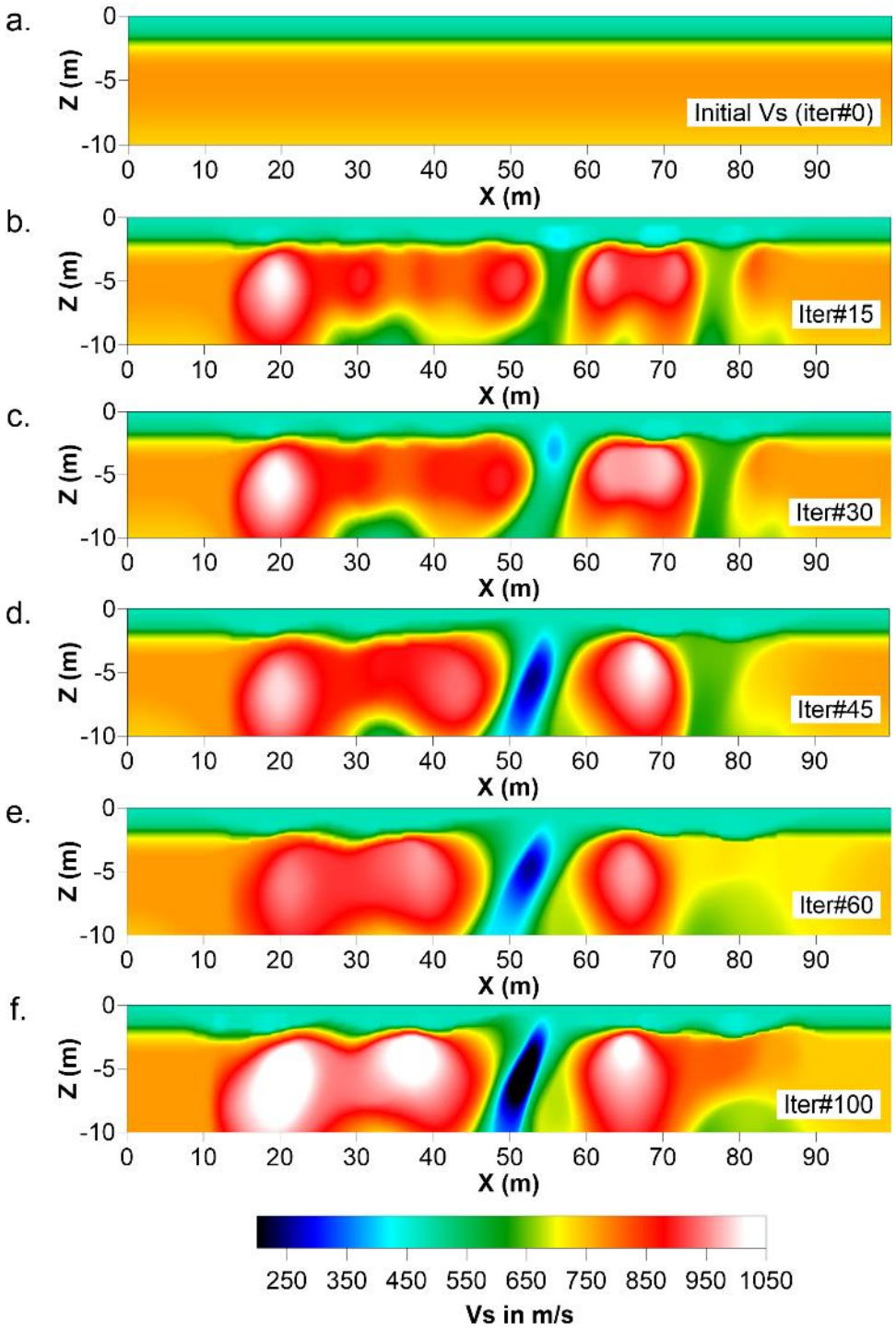

Figure 20. Inverted Vs profiles by the conventional FWI using pre-processed data. (a) Initial Vs model. Inverted Vs profiles are displayed for the (b) 15th, (c) 30th, (d) 45th, (e) 60th , and (f) 100th iteration.

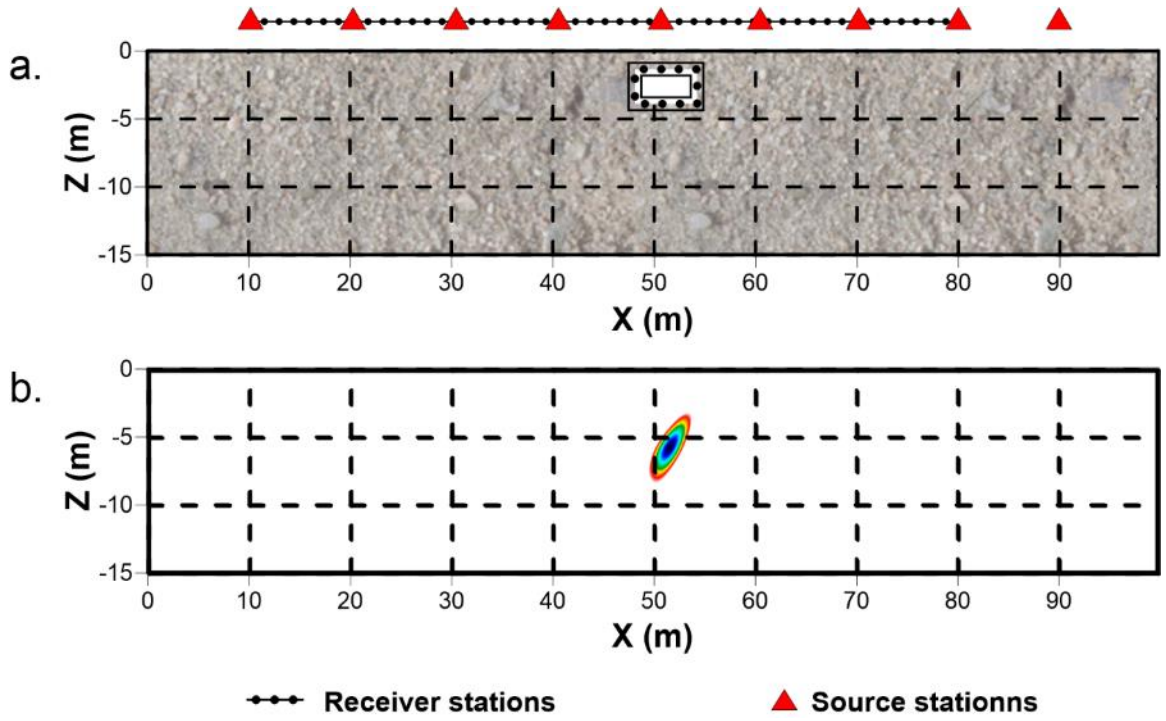

Figure 21. Conventional FWI detection result. (a) Location of the tunnel. (b) Detected location (Vs < 300 m/s) by conventional FWI using pre-processed data.

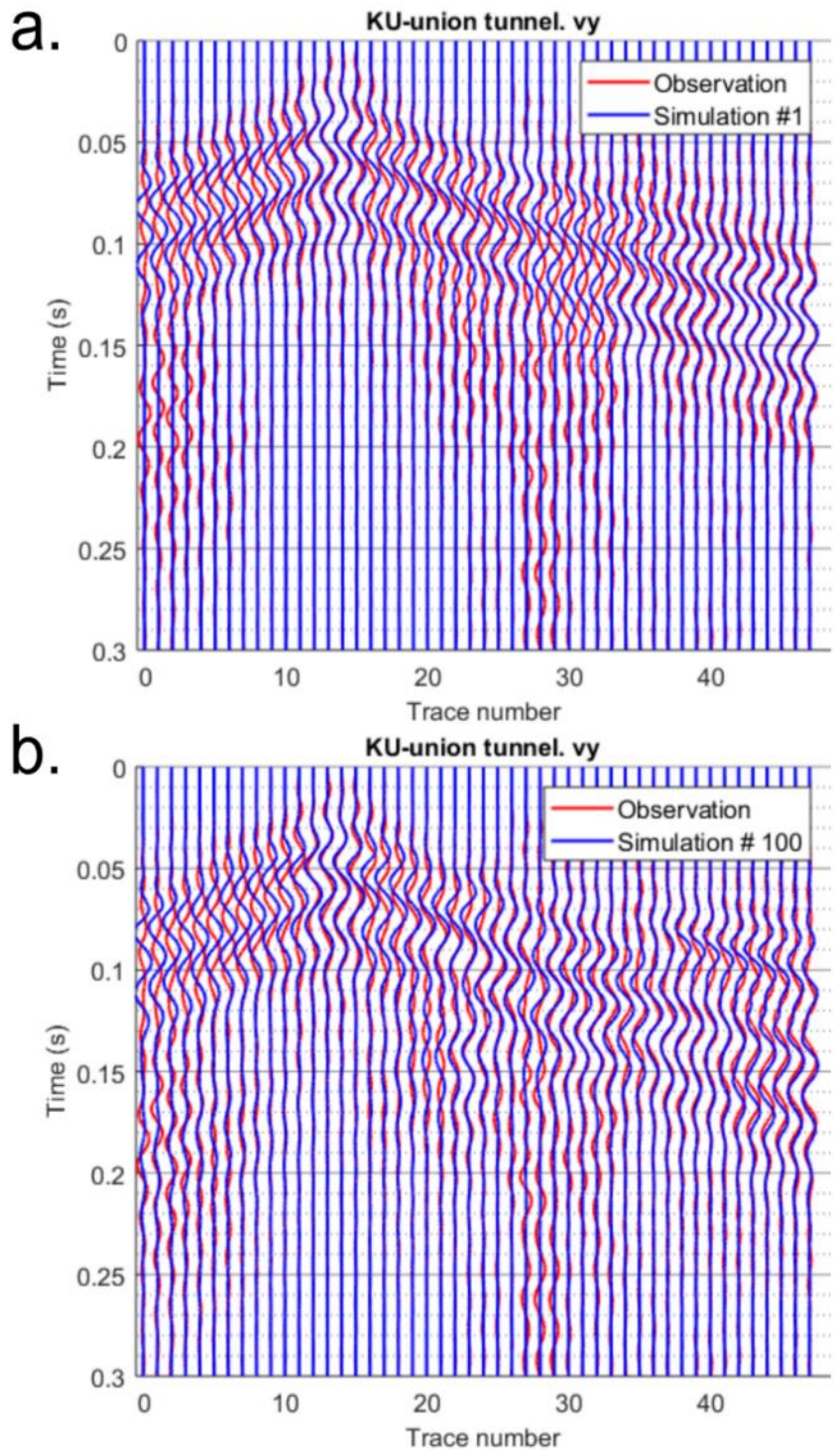

Figure 22. Waveform comparison for conventional FWI using pre-processed data at the (a) 1st iteration and the (b) 100th iteration. Red curves are the observed waveforms and blue curves are the synthetic waveforms.

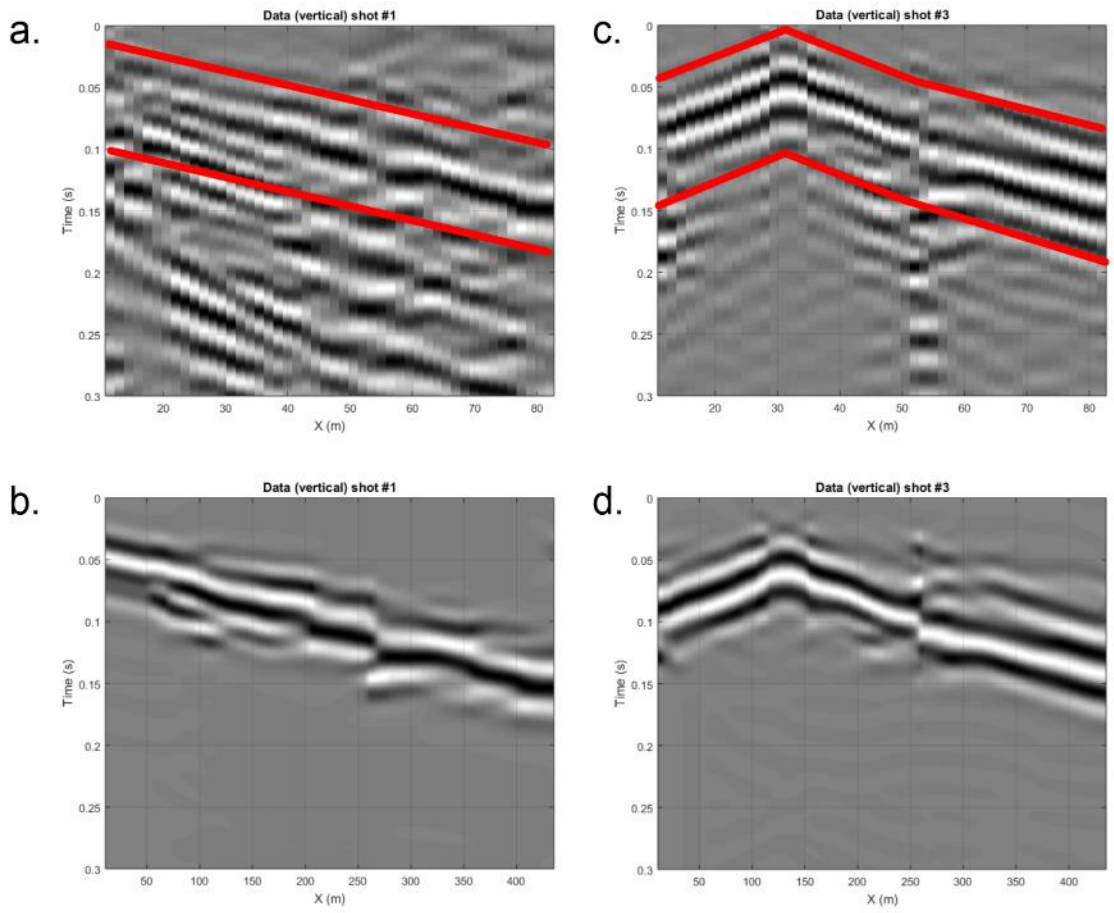

Figure 23. Time domain window functions (Tapers) applied to the pre-processed data. (a) Pre-processed data of record #1. Red lines are indicating the start- and end-point of the window functions. (b) Tapered data of record #1. (c) Pre-processed data of record #3. Red lines are indicating the start- and end-point of the window functions. (d) Tapered data of record #3.

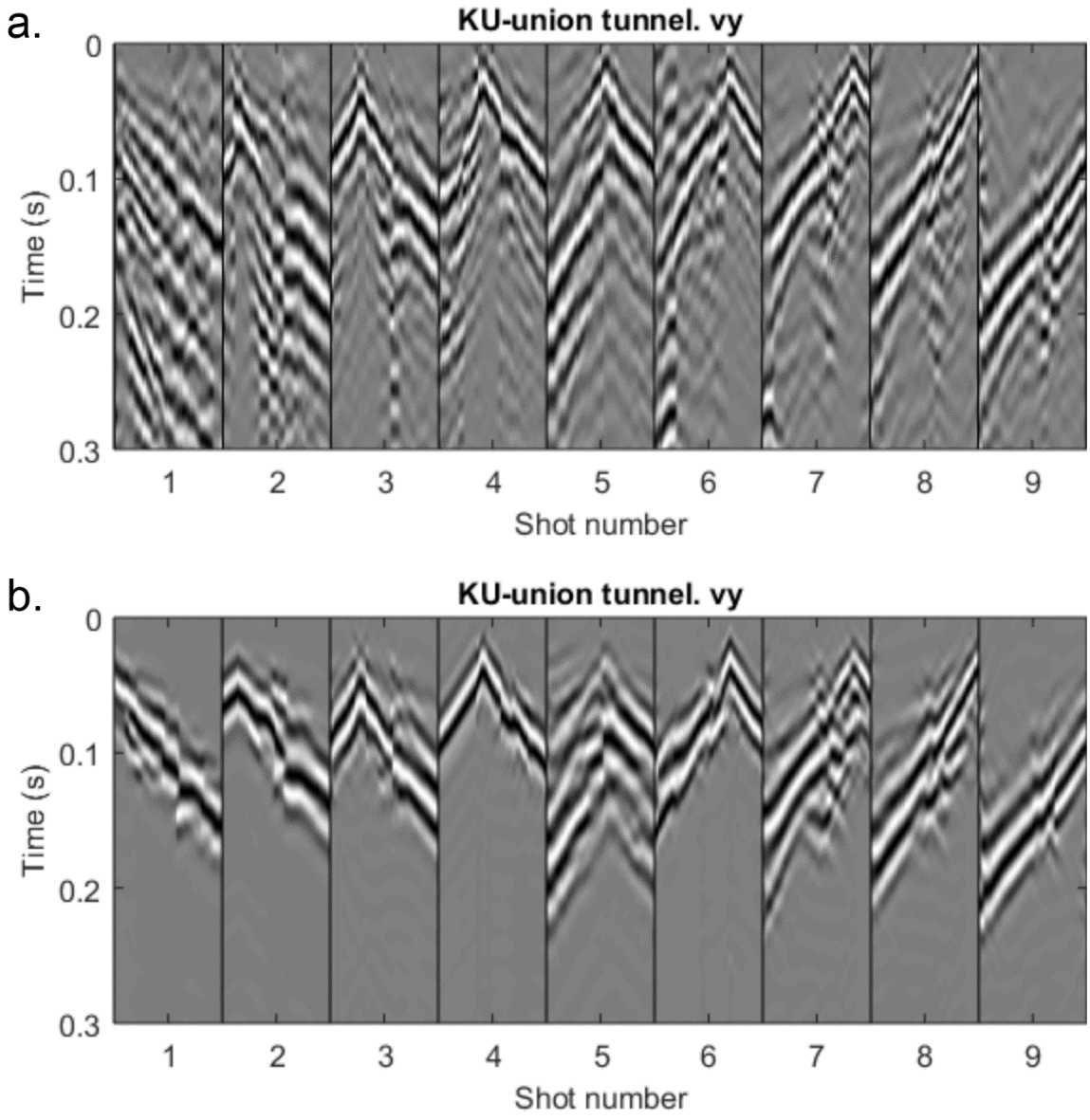

Figure 24. Comparison of (a) pre-processed data and (b) tapered data.

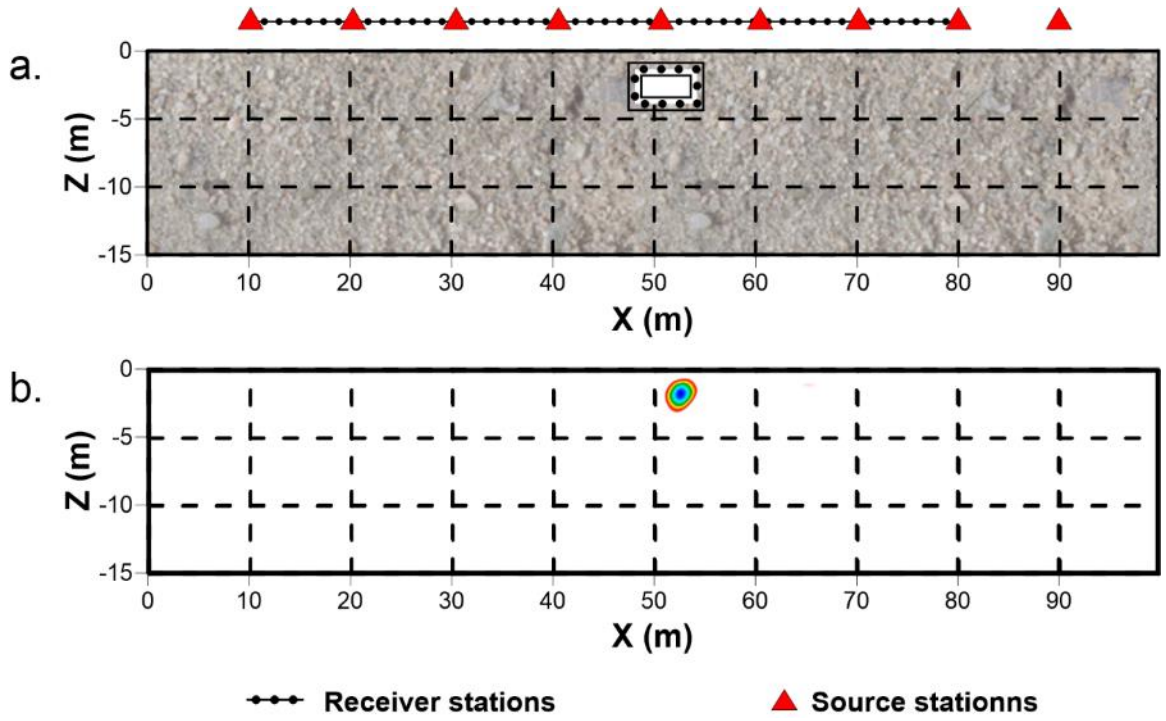

Figure 25. Improved conventional FWI detection result. (a) Location of the tunnel. (b) Detected location (Vs < 300 m/s) by conventional FWI using tapered data.

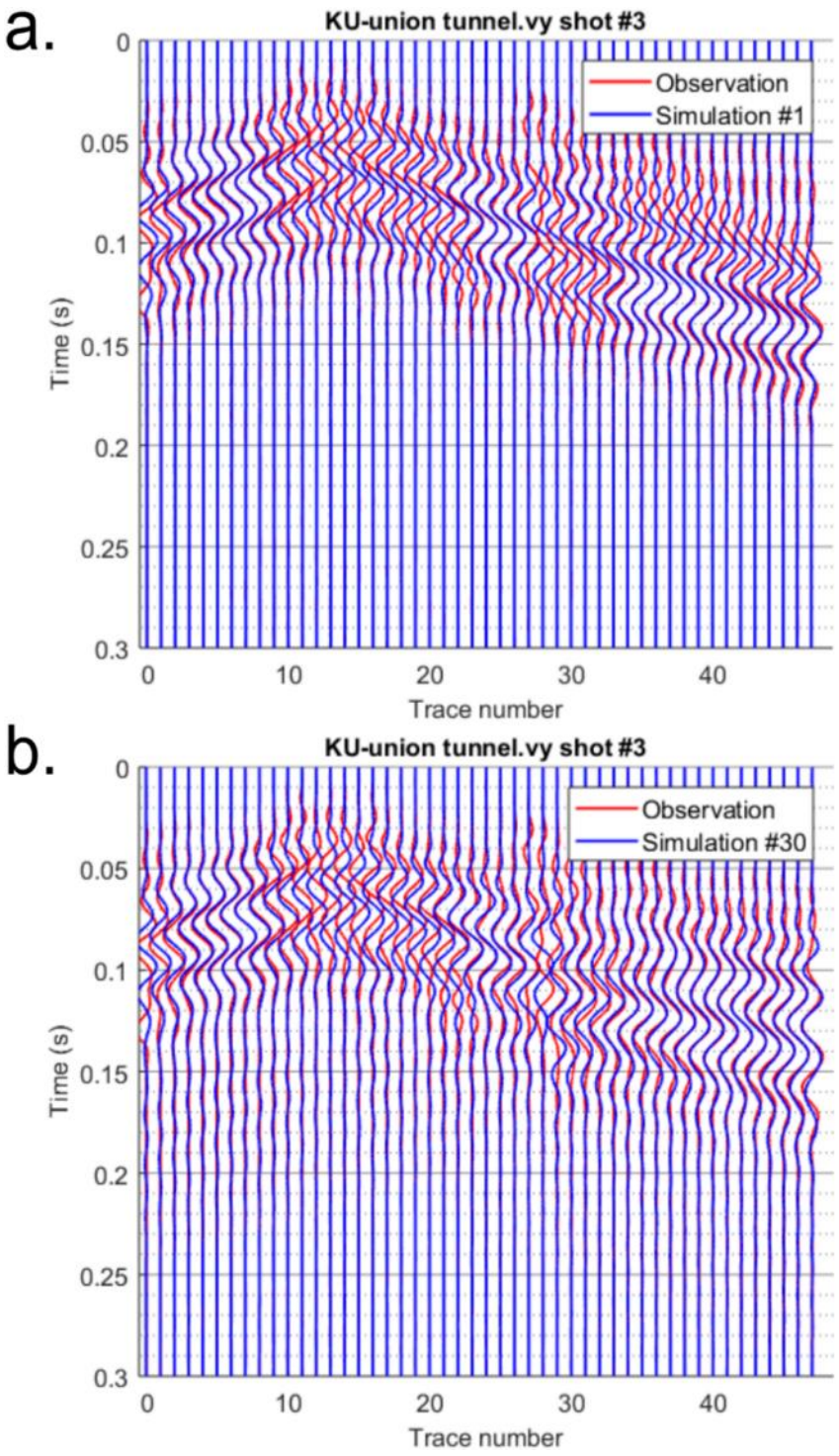

Figure 26. Waveform comparison for conventional FWI using tapered data at the (a) 1st iteration and the (b) 30th iteration. Red curves are the observed waveforms and blue curves are the synthetic waveforms.

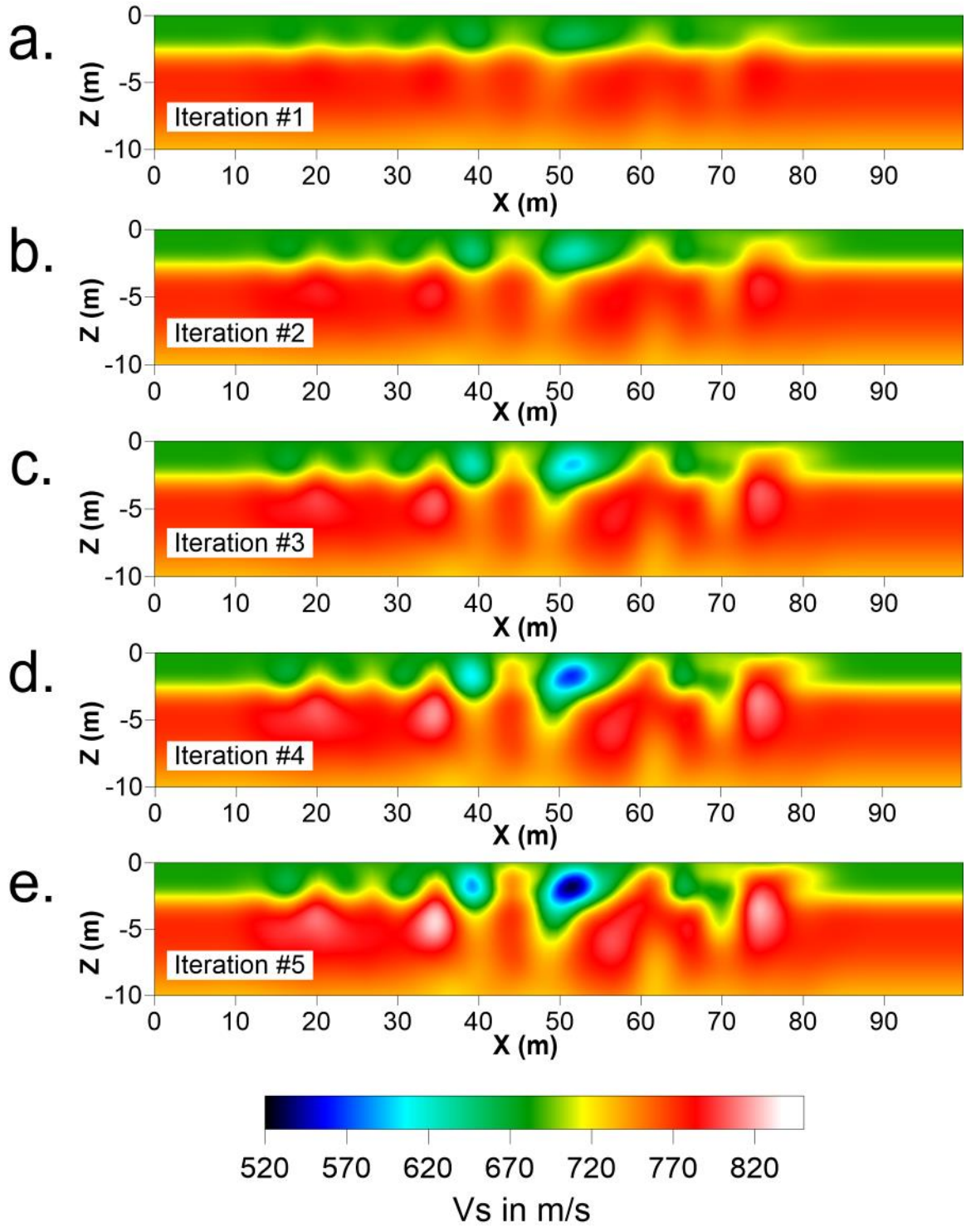

Figure 27. Inverted Vs profiles by BSWI using pre-processed data at the (a) 1st, (b) 2nd, (3) 3rd, (4) 4th, and (5) 5th iteration.

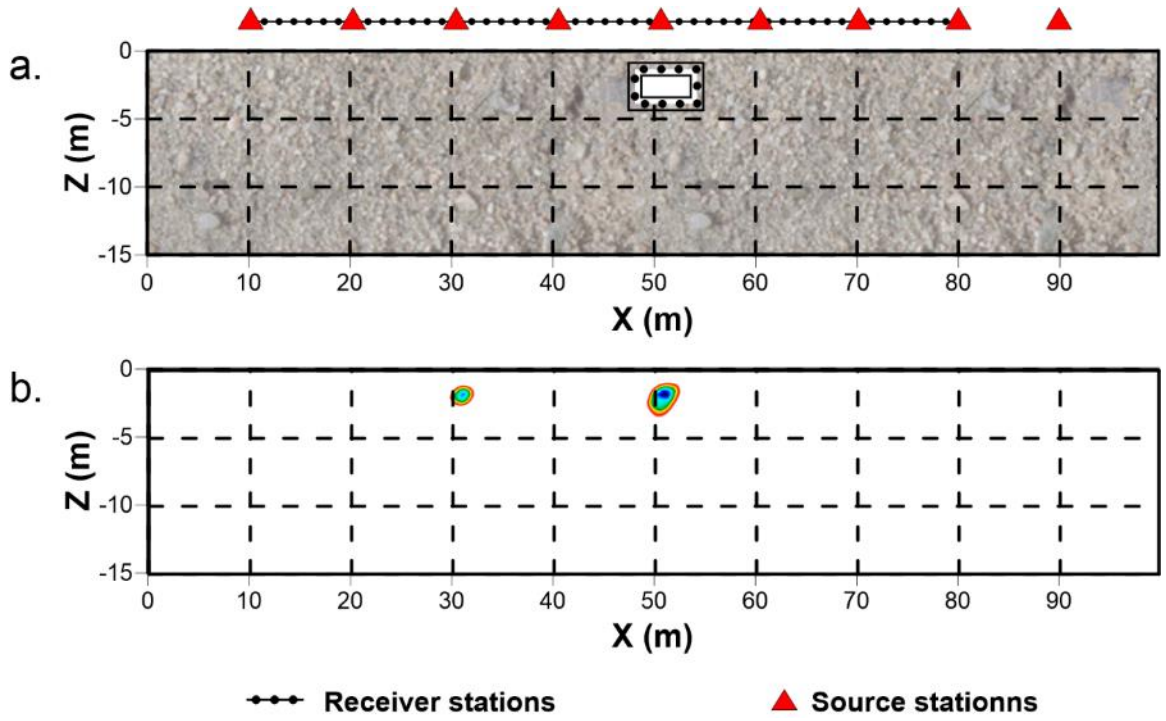

Figure 28. BSWI detection result. (a) Location of the tunnel. (b) Detected location (Vs < 300 m/s) by BSWI using pre-processed data.

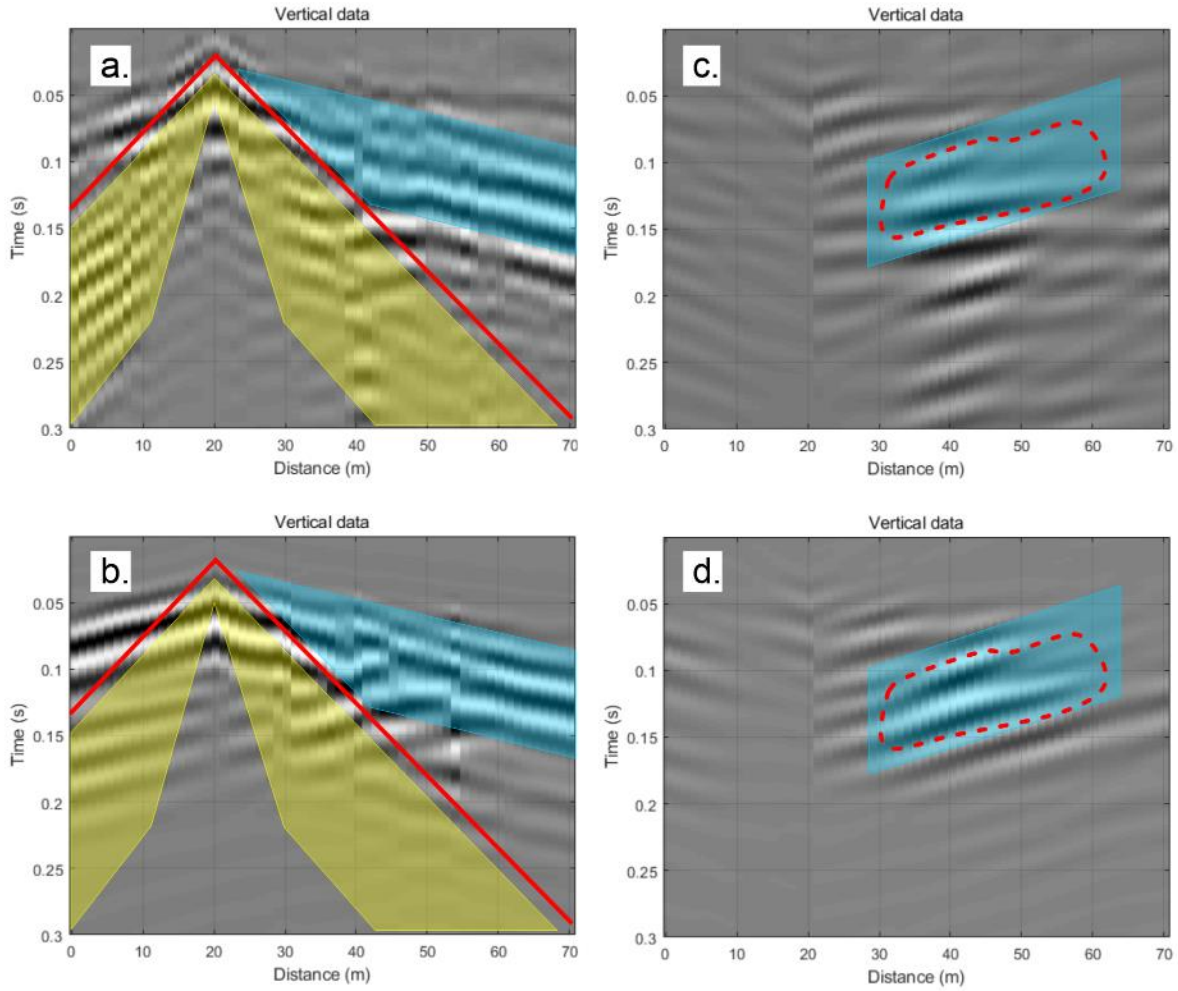

Figure 29. Waveform comparisons for record #3 at 30th iteration of the BSWI. The right panels are the slope-filtered records. a) Pre-processed data. b) Simulations at 30th iteration. c) Pre-processed data with slope filtering. d) Simulations at 30th iteration with slope filtering.

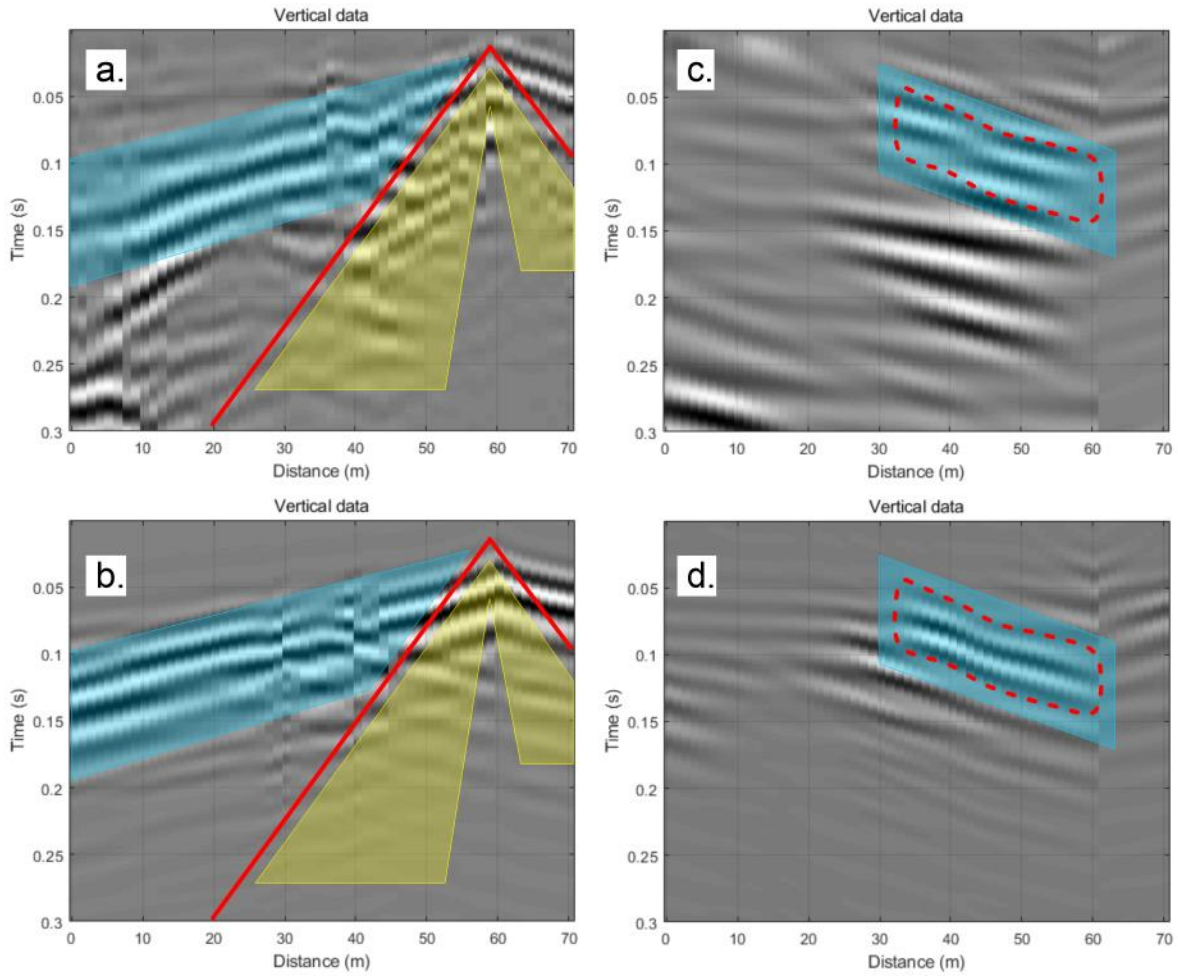

Figure 30. Waveform comparisons for record #7 at the 30th iteration of the BSWI. The right panels are the slope-filtered records. a) Pre-processed data. b) Simulations at 30th iteration. c) Pre-processed data with slope filtering. d) Simulations at 30th iteration with slope filtering.

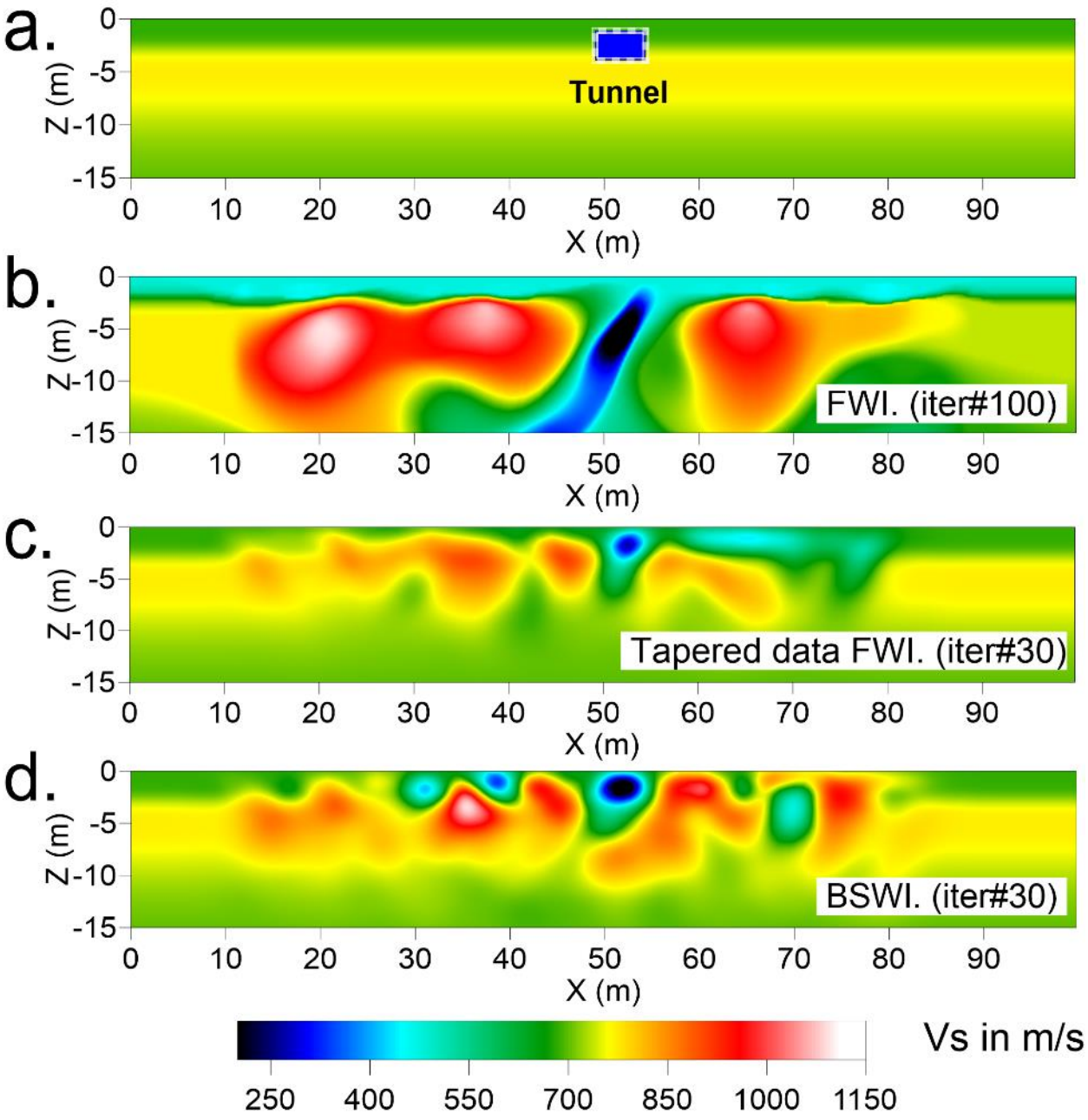

Figure 31. a) The initial Vs with the true location of the tunnel highlighted. b) The inverted Vs profile by conventional FWI of the pre-processed data after 100 iterations. c) The inverted Vs profile by conventional FWI of the tapered data after 30 iterations. d) The inverted Vs profile by the BSWI method of the pre-processed data after 30 iterations.

References

Almuhaidib, A. M., & Toksöz, M. N. (2014). Numerical modeling of elastic-wave scattering by near-surface heterogeneities. *Geophysics*, *79*(4), T199–T217.

Amrouche, M., & Yamanaka, H. (2014). Two-dimensional shallow soil profiling using time-domain waveform inversion. *Geophysics*, *80*(1), EN27–EN41.

Born M, W. E. (1964). *Principles of optics*. Oxford: Pergamon Press.

Chen, J., Zelt, C. A., & Jaiswal, P. (2016). Detecting a known near-surface target through application of frequency-dependent traveltime tomography and full-waveform inversion to P-and SH-wave seismic refraction data. *Geophysics*, *82*(1), R1–R17.

Dou, S., & Ajo-Franklin, J. B. (2014). Full-wavefield inversion of surface waves for mapping embedded low-velocity zones in permafrost. *Geophysics*, *79*(6), EN107–EN124.

Freund, L. B. (1998). *Dynamic fracture mechanics*. Cambridge university press.

Gubernatis, J. E., Domany, E., Krumhansl, J. A., & Huberman, M. (1977). The Born approximation in the theory of the scattering of elastic waves by flaws. *Journal of Applied Physics*, *48*(7), 2812–2819.

Hudson, J. A., & Heritage, J. R. (1981). The use of the Born approximation in seismic scattering problems. *Geophysical Journal International*, *66*(1), 221–240.

Ivanov, J., Schwenk, J. T., Peterie, S. L., & Xia, J. (2013). The joint analysis of refractions with surface waves (JARS) method for finding solutions to the inverse refraction problem. *The Leading Edge*, *32*(6), 692–697.

Jacob, K. H. (1970). Three-dimensional seismic ray tracing in a laterally heterogeneous spherical earth. *Journal of Geophysical Research*, *75*(32), 6675–6689.

Klessig, R., & Polak, E. (1972). Efficient Implementations of the Polak–Ribière Conjugate Gradient Algorithm. *SIAM Journal on Control*, *10*(3), 524–549.

Komatitsch, D., & Martin, R. (2007). An unsplit convolutional perfectly matched layer improved at grazing incidence for the seismic wave equation. *Geophysics*, *72*(5), SM155–SM167.

Koulakov, I., Stupina, T., & Kopp, H. (2010). Creating realistic models based on combined forward modeling and tomographic inversion of seismic profiling data. *Geophysics*, *75*(3), B115–B136.

Levander, A. R. (1988). Fourth-order finite-difference P-SV seismograms. *Geophysics*, *53*(11), 1425–1436.

Livers*, A. J., Peterie, S. L., Ivanov, J., & Miller, R. D. (2015). Feasibility of parallel line beamsteering for enhanced tunnel detection. In *SEG Technical Program Expanded Abstracts 2015* (pp. 2292–2297). Society of Exploration Geophysicists.

Mora, P. (1987). Nonlinear two-dimensional elastic inversion of multioffset seismic data. *Geophysics*, *52*(9), 1211–1228.

Nocedal, J., & Wright, S. J. (1999). *Numerical Optimization ${$Springer Series in Operations Research$}$*. Springer-Verlag New York Incorporated.

Park, C. B., Miller, R. D., & Xia, J. (1999). Multichannel analysis of surface waves. *Geophysics*, *64*(3), 800–808.

Park, C. B., Miller, R. D., Xia, J., & Ivanov, J. (2007). Multichannel analysis of surface waves (MASW)—active and passive methods. *The Leading Edge*, *26*(1), 60–64.

Shao, G., Tsoflias, G. P., & Li, C. (2016). Detection of near-surface cavities by generalized S-transform of Rayleigh waves. *Journal of Applied Geophysics*, *129*, 53–65.

Sherman, C. S., Rector, J., Dreger, D., & Glaser, S. (2018). A numerical study of surface-wave-based tunnel detection at the Black Diamond Mines Regional Preserve, California. *Geophysics*, *83*(4), EN13–EN22.

Shipp, R. M., & Singh, S. C. (2002). Two-dimensional full wavefield inversion of wide-aperture marine seismic streamer data. *Geophysical Journal International*, *151*(2), 325–344.

Sloan, S. D., Peterie, S. L., Ivanov, J., Miller, R. D., McKenna, J. R., Bradford, J. H., & Holliger, K. (2010). Void detection using near-surface seismic methods. *Advances in Near-Surface Seismology and Ground-Penetrating Radar: SEG Geophysical Developments Series*, *15*, 201–218.

Sloan, S. D., Peterie, S. L., Miller, R. D., Ivanov, J., Schwenk, J. T., & McKenna, J. R. (2015). Detecting clandestine tunnels using near-surface seismic techniques. *Geophysics*, *80*(5), EN127–EN135.

Smith, J. A., Borisov, D., Cudney, H., Miller, R. D., Modrak, R., Moran, M., … Wang, Y. (2018). Tunnel detection at Yuma Proving Ground, Arizona, USA—Part 2: 3D full-waveform inversion experiments. *Geophysics*, *84*(1), B95–B108.

Sourbier, F., Operto, S., Virieux, J., Amestoy, P., & L'Excellent, J.-Y. (2009a). FWT2D: A massively parallel program for frequency-domain full-waveform tomography of wide-aperture seismic data—Part 1: Algorithm. *Computers & Geosciences*, *35*(3), 487–495.

Sourbier, F., Operto, S., Virieux, J., Amestoy, P., & L'Excellent, J.-Y. (2009b). FWT2D: A massively parallel program for frequency-domain full-waveform tomography of wide-aperture seismic data—Part 2: Numerical examples and scalability analysis. *Computers & Geosciences*, *35*(3), 496–514.

Tarantola, A. (1984). Inversion of seismic reflection data in the acoustic approximation. *Geophysics*, *49*(8), 1259–1266.

Tarantola, A. (2005). *Inverse problem theory and methods for model parameter estimation* (Vol. 89). siam.

Tran, K. T., & Sperry, J. (2018). Application of 2D full-waveform tomography on land-streamer data for assessment of roadway subsidence. *Geophysics*, *83*(3), EN1–EN11.

Virieux, J. (1986). P-SV wave propagation in heterogeneous media: Velocity-stress finite-difference method. *Geophysics*, *51*(4), 889–901.

Virieux, J., & Operto, S. (2009). An overview of full-waveform inversion in exploration geophysics. *Geophysics*, *74*(6), WCC1–WCC26.

Wang, Y., Miller, R. D., Peterie, S. L., Sloan, S. D., Moran, M. L., Cudney, H. H., … Tromp, J. (2018). TUNNEL DETECTION AT YUMA PROVING GROUND, ARIZONA, USA. PART 1: 2D FULL-WAVEFORM INVERSION EXPERIMENT. *Geophysics*, *84*(1), 1–44.

Xia, J., Nyquist, J. E., Xu, Y., Roth, M. J., & Miller, R. D. (2007). Feasibility of detecting near-surface feature with Rayleigh-wave diffraction. *Journal of Applied Geophysics*, *62*(3), 244–253.

Yuan, Y. O., Simons, F. J., & Bozdağ, E. (2015). Multiscale adjoint waveform tomography for surface and body waves. *Geophysics*, *80*(5), R281–R302.